May 1999

Search for $\mu^+ \to e^+\gamma$ down to 10^{-14} branching ratio

Research Proposal to Paul Scherrer Institut

Institution	*Participant*
Budker Institute of Nuclear Physics Novosibirsk, Russia	Lev M. Barkov Andrey A. Grebenuk Boris I. Khazin Vladimir P. Smakhtin
International Center for Elementary Particle Physics, University of Tokyo Tokyo, Japan	Shoji Asai Tetsuro Mashimo Satoshi Mihara Toshinori Mori * Shuji Orito Takayuki Saeki Ikuo Ueda Satoru Yamashita Jun Yashima Koji Yoshimura
Institute of Particle and Nuclear Studies, KEK Tsukuba, Japan	Yoshitaka Kuno Akihiro Maki Yasuhiro Sugimoto Akira Yamamoto
Nagoya University Nagoya, Japan	Kimiaki Masuda
Waseda University Tokyo, Japan	Tadayoshi Doke Jun Kikuchi Hiroyuki Okada Satoshi Suzuki

* spokesperson

Contents

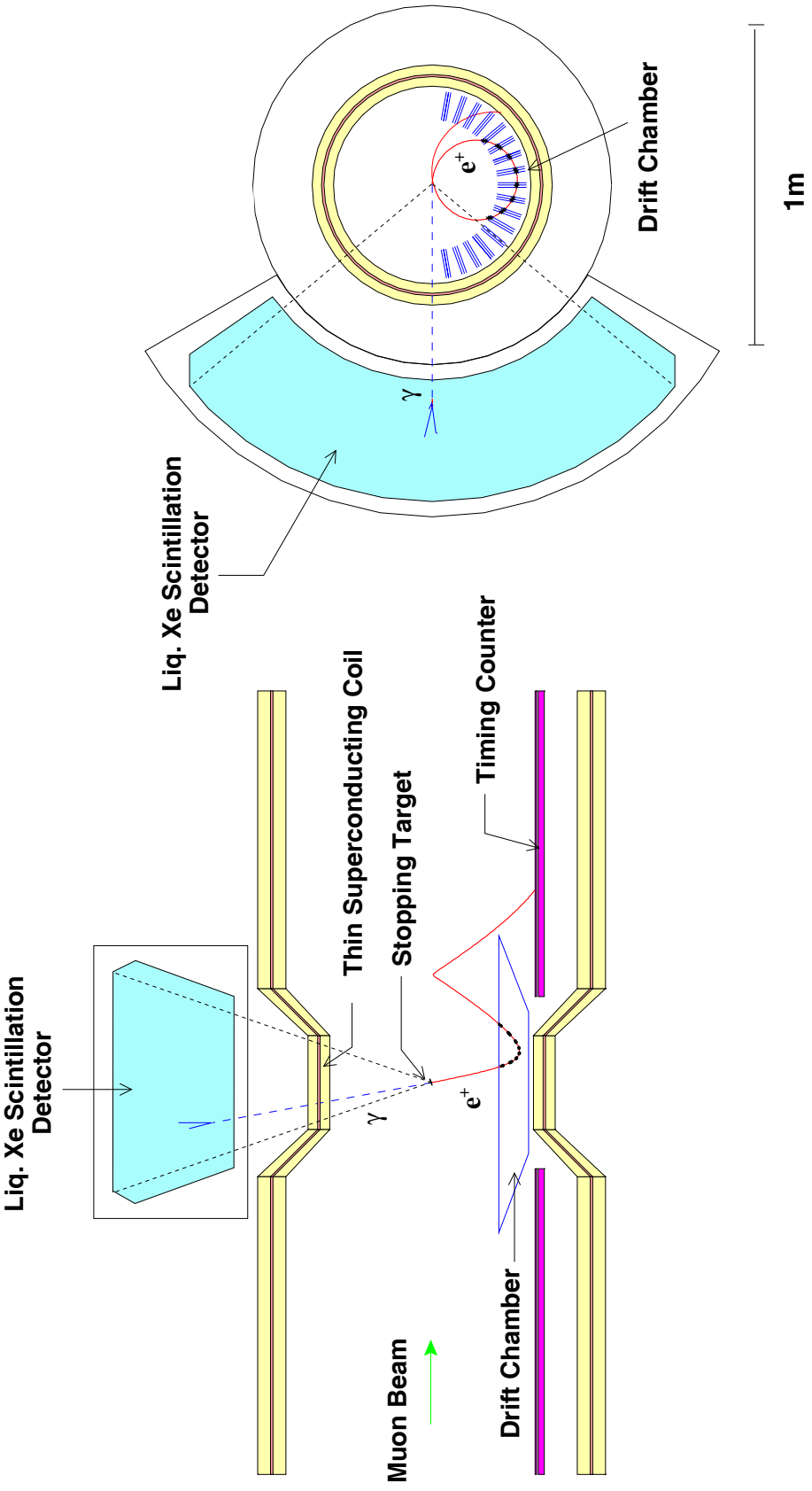

Figure 1: Schematic view of the detector

1 Summary of the Proposal

We propose to search for the lepton-flavor-violating decay $\mu^+ \to e^+\gamma$ with a sensitivity of 10^{-14}. The experiment will be conducted at PSI by using the πE5 beam, the most intense DC muon beam presently available in the world. Our intention is to utilize detector elements with best possible resolutions both on the e^+- and γ-sides, so that a background-free identification of the signal down to this small branching ratio can be obtained hopefully with a good margin.

Fundamental theories such as supersymmetric unification seem to generically predict [1] that $\mu^+ \to e^+\gamma$ occurs with a decay branching ratio somewhere above 10^{-14}. We therefore consider that this experiment has a real chance of making a discovery, which will provide a stunning evidence for new physics beyond the standard model.

Even the non-observation of the decay at this sensitivity will provide a stringent constraint on the fundamental theories and on the general natures of the new physics, and thus will be of crucial importance in pointing future direction of the particle physics.

Recent discovery of the neutrino oscillation by Super Kamiokande [2] increases the importance of this search perhaps tremendously. The see-saw mechanism [3] induced by superheavy (10^{12} – 10^{15}GeV) right-handed Gauge singlets (ν_{R_i}) is considered to be a most promising candidate to explain the origin of the extremely small neutrino masses, measured by Super Kamiokande. It is pointed out [4] that the off-diagonal slepton mass-matrices, also induced by the same right-handed singlets, will significantly contribute to the $\tau \to \mu\gamma$ and $\mu \to e\gamma$ decay rates.

It is further shown [4] that $\mu^+ \to e^+\gamma$ branching ratio will determine or severely constrain the mass scale of the right-handed singlet ν_{R_2}, when combined with the Δm^2 and the mixing angle between ν_μ and ν_e, to be measured by the solar neutrino experiments. Therefore, $\mu^+ \to e^+\gamma$ decay can be the unique window to observe the isolated world of the right-handed Gauge singlets, postulated to exist at ultra high energies.

The sensitivity (1×10^{-14}) we aim is three orders of magnitudes below the limit recently set by MEGA experiment [5]. In the frame work of the theories mentioned above, our sensitivity on $\mu^+ \to e^+\gamma$ corresponds [6] to a sensitivity of 2.5×10^{-17} on the $\mu-e$ conversion process with the aluminum target, very similar to the sensitivity MECO proposal aims to reach [7].

A schematic view of the detector we propose is shown in Fig. 1.

A muon beam of intensity 1×10^8/sec with small emittances is created from the πE5 beam by a combination of collimators, degraders and a beam transport solenoid, and is brought to stop in a thin target.

The momentum and the direction of the emerging e^+ are measured precisely by a "COnstant-Bending-RAdius (COBRA) spectrometer," composed of a solenoidal magnetic field with a field gradient. The field is arranged such that monochromatic e^+s from the target follow trajectories with constant projected bending radius, independent of the emission angle over a wide angular range. This allows us to sharply define the absolute momentum window of e^+ to be detected by drift chamber cells placed at outer most radii, thereby reducing the accidental pile-up of the Michel e^+ much more effectively than is possible with a simple solenoidal configuration employed by MEGA. This new feature, together with the special arrangement of the drift chamber cells, make the pattern-recognition secure against the pile-up, specially with our beam rate, which is a factor 2.5 below the instantaneous beam rate (2.5×10^8/sec) MEGA had taken.

Simulation shows the expected FWHM resolutions of 0.7% for the positron momentum and 9 mrad for the angle.

A hodoscope array of plastic scintillators is placed on each side of the spectrometer to measure the impact point and the timing of the e^+ with resolution (FWHM) of 2 cm and 0.1 nsec, respectively.

While all e^+ are confined inside the magnet by the bending, the gamma rays penetrate through the thin superconducting coil of the spectrometer with 95% transmission probability, and are detected by a liquid Xenon scintillation detector of "Mini-Kamiokande" type, which is a 0.8 m^3 volume of liquid Xe viewed by arrays of total 800 photomultipliers from all sides. We use only the scintillation light, and do not attempt to collect the ionization. Thus our photon detector is very simple. The scintillation pulse from the Xe is very fast and has a short tail, thereby minimizing the pile-up problem, which can further be reduced by off-line analyses of the image-pattern and the pulse-shapes. Construction and long-term operation of a prototype have been very successful. Tests on the prototype and a full simulation show that one can expect, for 52.8 MeV γ rays, FWHM resolutions of 1.4% for the energy-, 4 mm for the position- and better than 0.1 nsec for the timing-measurements.

Detailed studies and simulations indicate that we can reduce the background well below our sensitivity, with all these features of the detector. We fully realize that the experiment is a difficult one. At the same time, we are confident that we can conduct the experiment and arrive at the sensitivity. This confidence is based on our past experiences of performing various projects ranging from collider to balloon-borne experiments, in which most of the detector elements we propose were actually used.

We request a total of 6,000 hours of beam time starting in year 2003 with a proton intensity above 1 mA. Tests and engineering runs with πE5 will be requested in years 2000 to 2002. A dedicated in-house group of physicists and engineers at PSI will be a necessity.

The collaboration invites scientists who share common physics interests and detector strategies to join this project.

2 Physics Motivation

2.1 Overview

In the Standard Model, lepton flavor conservation (LFC) is built in by hand with assumed vanishing neutrino masses. Introduction of neutrino masses and their mixing into the standard model also predicts unmeasurably small lepton flavor violation (LFV). On the other hand, fundamental theories such as supersymmetry generically predict LFV at a measurable level. Lepton-flavor-violating processes such as $\mu^+ \to e^+\gamma$ are therefore very clean, (i.e. not contaminated by the background of the Standard Model), and at the same time compose a promising area to hunt for signals of profound new physics.

2.2 Supersymmetric Grand Unified Theory

LFV processes are specially sensitive to the supersymmetric (SUSY) extension of the Standard Model, in particular supersymmetric grand unified theories (SUSY-GUT). In SUSY-GUT, finite slepton mixing appears through radiative corrections in the renormalization group evolution from the GUT to the weak energy scale, even if the slepton mass matrix is assumed to be diagonal at the Plank scale [8]. Recently, it was pointed out that the slepton mixing thus generated can be very large owing to the heavy top-quark mass [1], thereby enhancing $\mu^+ \to e^+\gamma$ decay through loop diagrams shown in Fig. 2. The predicted branching ratio of $\mu^+ \to e^+\gamma$ in

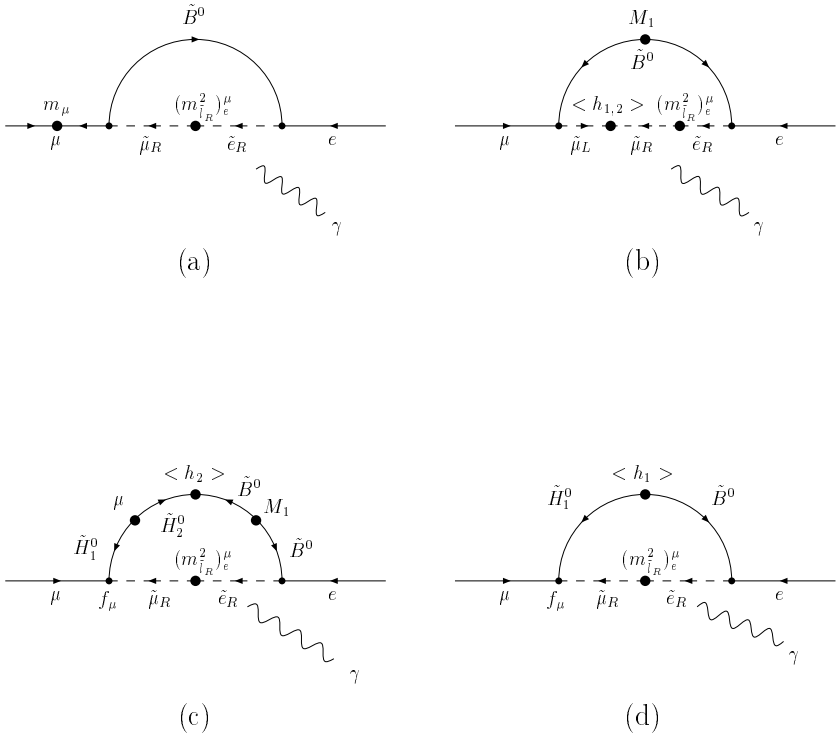

Figure 2: Diagrams of $\mu^+ \to e^+\gamma$ in SU(5) SUSY models.

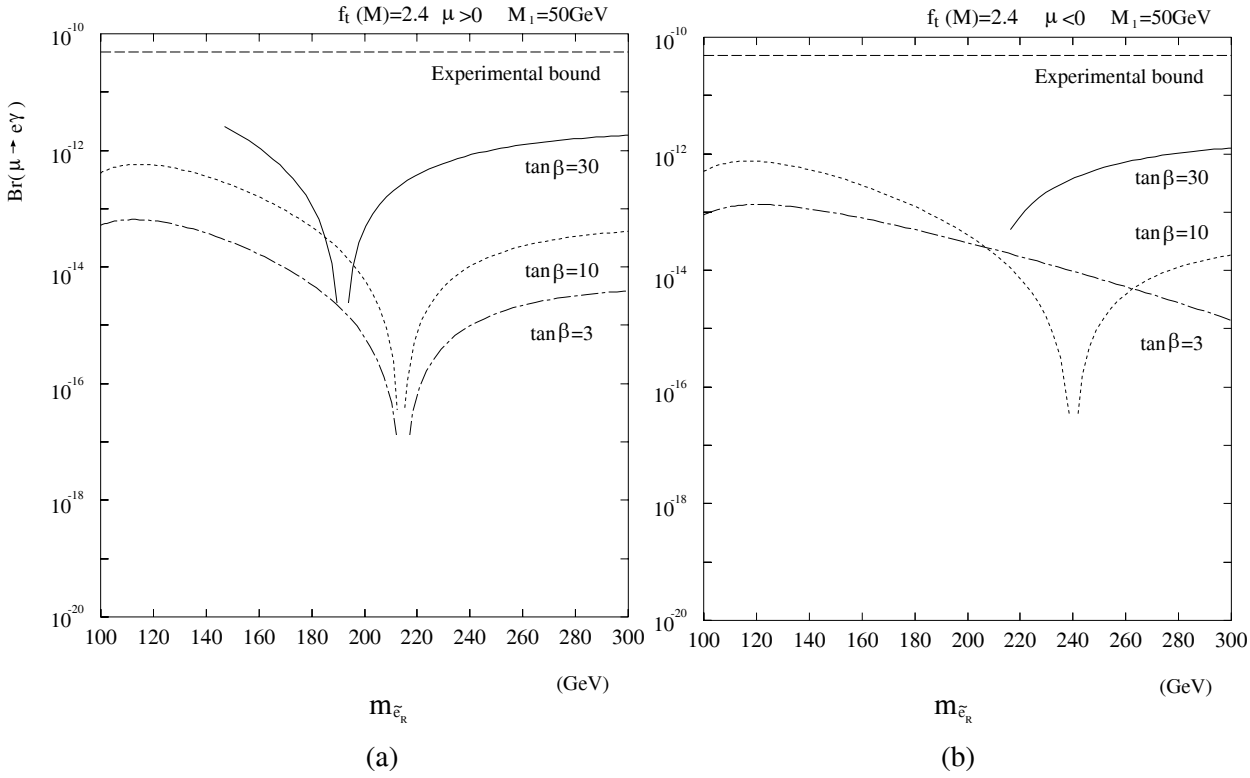

Figure 3: Predictions of $\mu^+ \to e^+\gamma$ branching ratio in SU(5) SUSY models [8]. The new limit of 1.2×10^{-11} recently reported by MEGA [5] is not shown.

SUSY SU(5) models [9] is shown in Fig. 3. It ranges from 10^{-15} to 10^{-13} for the singlet smuon mass $m_{\tilde{\mu}_R}$ of 100 to 300 GeV. The SO(10) SUSY-GUT models predict an even larger value of 10^{-13} to 10^{-11} by an enhancement factor of $(m_\tau^2/m_\mu^2) \sim 100$ [1], induced by the loop diagrams whose magnitude is proportional to the tau-lepton mass.

2.3 Connection with the Neutrino Oscillations

Over last 20 years, there have been growing evidences for the solar neutrino deficit [10, 11, 12], which is most likely to be explained by the neutrino oscillation. Super Kamiokande has finally discovered the oscillation of the atmospheric neutrino [13], thereby making a breakthrough in the particle physics. The neutrino oscillation implies both non-zero neutrino masses and LFV. In SUSY models, these neutrino mixing is expected to enhance the rate of LFV processes such as $\mu^+ \to e^+\gamma$ [4, 14, 15].

A possible contribution to the slepton mixing between $\tilde{\mu}$ and $\tilde{e}$ is from V_{21} (between ν_1 and ν_2), corresponding to the mixing for solar neutrino deficit. Data on solar neutrino now seem to confine the mixing parameters to several allowed regions, namely the MSW large-angle solution, the MSW small-angle solution and the vacuum oscillation, as shown in the left plot in Fig. 4. The right plot in Fig. 4 shows the predictions for $\mu^+ \to e^+\gamma$ decay corresponding to the three solutions as a function of the mass of the right-handed Gauge singlet ν_{R_2}

Therefore, the $\mu^+ \to e^+\gamma$ branching ratio, when combined with Δm^2 and mixing angle measurements by solar neutrino experiments, will determine or severely constrain the mass scale of the right-handed Gauge singlet, postulated to exist at ultra high energies ($10^{12} \sim 10^{15}$ GeV).

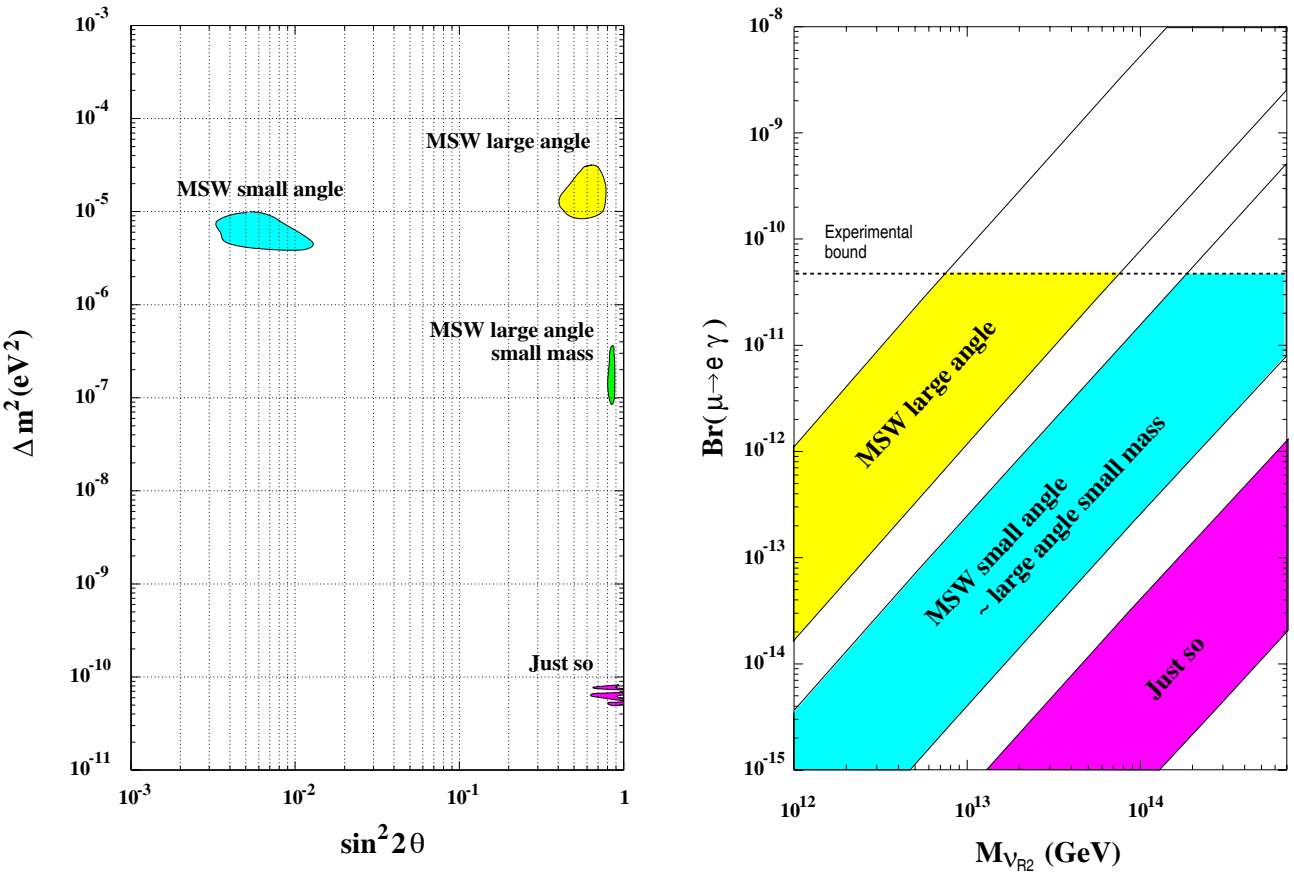

Figure 4: Possible solutions for neutrino oscillation (left) and corresponding $\mu^+ \to e^+\gamma$ branching ratios (right) as a function of the mass of the right-handed Gauge singlet ν_{R_2}.

3 Detector

3.1 Beam and Target

The πE5 channel [16] extracts low-energy π and μ beams from the thick production target at an angle of 175° with respect to the primary proton beam. The main characteristics of the beam are listed in Table 1. For the $\mu \to e\gamma$ experiment the beam channel will be tuned to $\approx$ 28 MeV/c to collect the surface muons. Measurements indicate that we can expect beam intensity up to $8 \sim 10 \times 10^8 \mu$/sec for the primary proton current of 1.5mA [16].

Table 1: Main properties of πE5.

solid angle acceptance	150 msr
momentum range	20–120 MeV/c
length	10.4 m
momentum band (FWHM)	10%
momentum resolution (FWHM)	2%
horizontal emittance	15.3 cm·rad
vertical emittance	3.6 cm·rad
spot size	4×4 cm^2

Fig. 5 shows the beam line and layout of the experimental areas. The beam line consists of a chain of bending, quadrapole and hexapole magnets. In the middle of the beam line, there are horizontal and vertical slits which define the momentum and/or the acceptance. There are

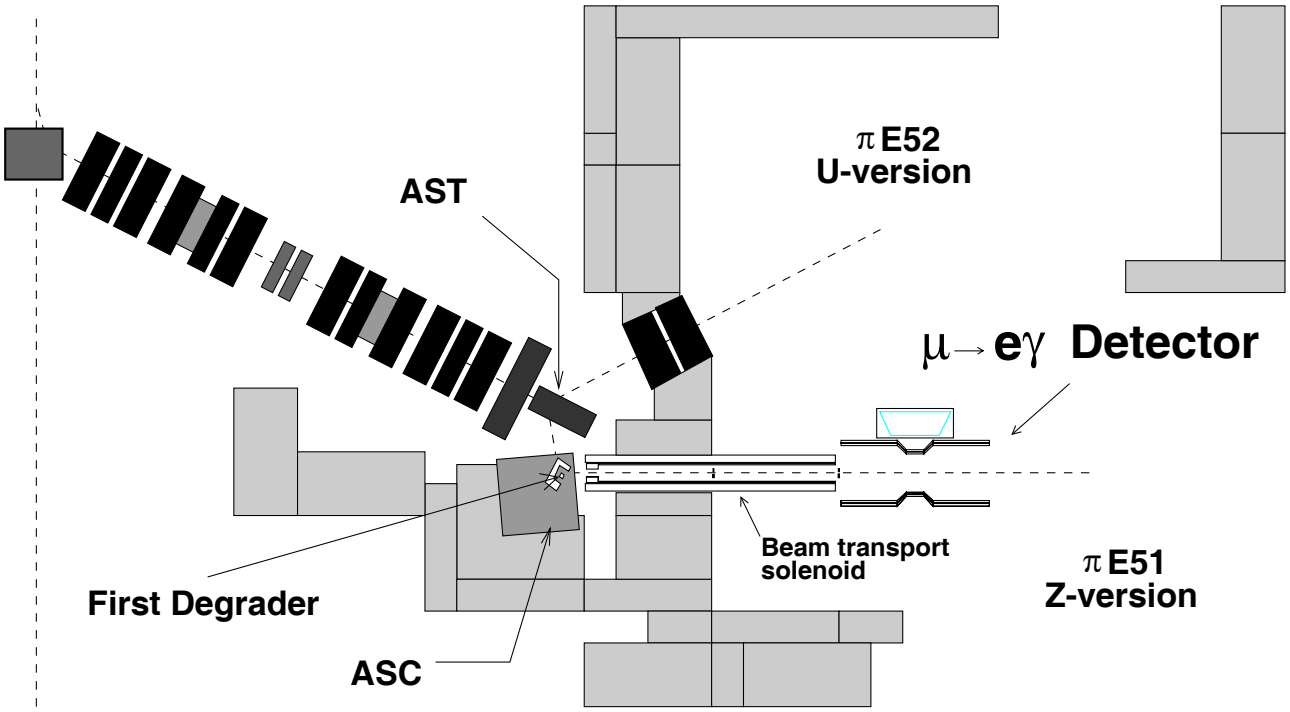

Figure 5: The layout of πE5

two modes of operation, "U" and "Z", feeding the areas πE52 and πE51, respectively. The two modes are switched by the second bending magnet (AST) located at the end of the line.

The aim of our beam transport design is to obtain a muon beam of acceptable intensity ($1 \sim 2 \times 10^8$/sec) with a minimum spot-size and a small momentum spread finally at the stopping target of our experiment. Studies and optimization are performed by using TRANSPORT [17] and GEANT [18], starting with the beam phase-space data supplied by PSI. We here concentrate on Z-mode, while studies on U-mode are under way.

An example of solutions found is shown in Fig. 5 and Fig. 6. For the Z-mode, the image of the production target is reproduced at the center of the last bending magnet (ASC), where we install a degrader of 500 μm thick mylar. The muons lose much more energy in the degrader than the background positrons in the beam, and are bent more in the second half of the bending magnet. A collimator (C1) of 14 cm diameter blocks out the positrons and, at the same time,

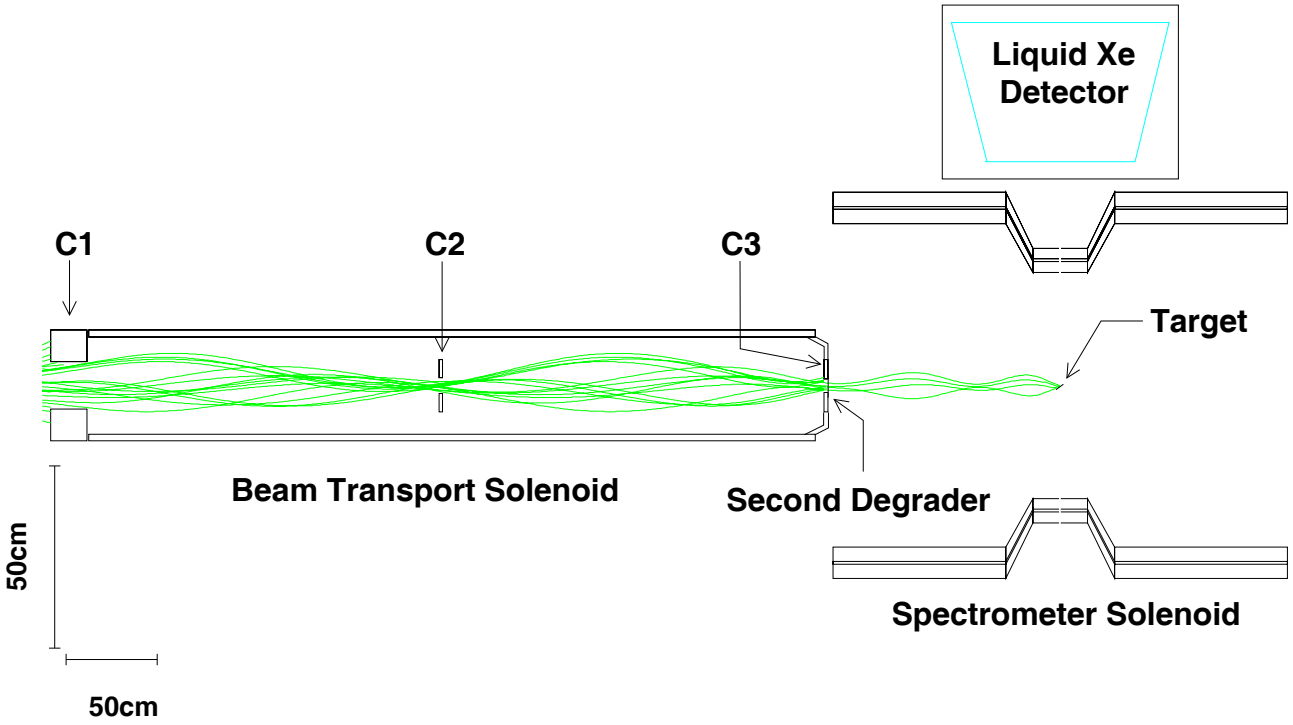

Figure 6: Transportation of μ^+ beam to the target. Note the vertical scale is expanded by a factor two as compared to the horizontal scale.

selects a best part of the muon beam emittance. A solenoid of 30 cm diameter and 4 m length transports the muon beam with its 0.2 Tesla field. Beam halos can further be scraped by placing second collimator (C2) at the first focal point in the solenoid. At the exit of the solenoid, which is the second focal point, the beam is further degraded by a 50 μm thick mylar vacuum window, and can be scraped again by a collimator (C3 with a diameter of 4 cm), which also serves as a circular frame to support the mylar window.

The target region is filled with He gas, in which a stopping target of 100 μm thick mylar is placed with a slant angle of 22^o (corresponding to a slant ratio of 1:2.5). Fig. 7 shows the beam profile at the target. The beam has a very small size with rms spread of 5 mm in σ_x and σ_y. Fig. 8 shows the z-distribution of the muon stopping point. We have a negligible stopping

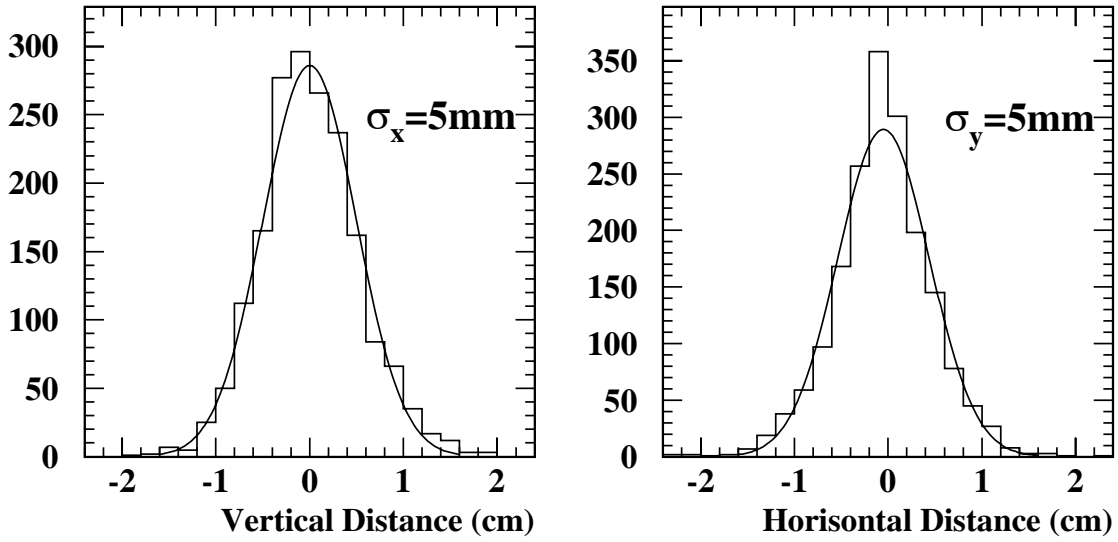

Figure 7: Vertical and horizontal μ^+ beam profile at the target.

rate in the helium gas. Fig. 9 shows the distribution of the stopping positions in the target (normal depth from the surface). About 50% of the μ^+ stops within 50 μm from the surface of the target, thereby minimizing the multiple scattering which emerging positrons suffer in the target.

For the solution described above, 19% of the full πE5 beam is brought to stop at the target, providing an intensity of $1 \sim 2 \times 10^8$ stop μ/sec for 1.5mA primary proton beam. Further tests on πE5 beam and transport studies will be likely to find even better solutions.

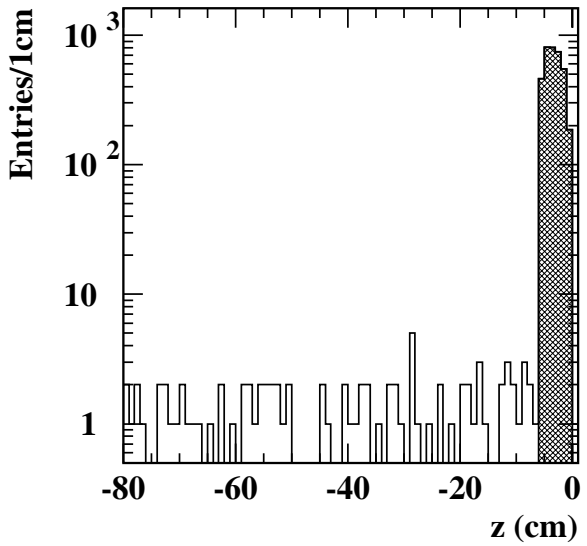

Figure 8: Stopping positions of μ^+s along the beam direction. The hatched histogram shows μ^+s which stop in the target.

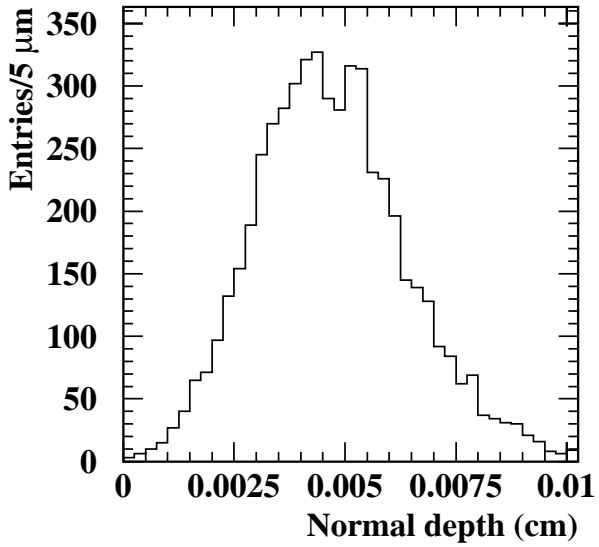

Figure 9: Stopping positions (normal depth from the surface) of μ^+ in the target.

3.2 Positron Spectrometer

3.2.1 Concept of COBRA Spectrometer

The positron spectrometer, schematically shown in Fig.10, consists of a magnet specially designed to form a gradient field, a drift chamber system to measure the positron momentum, and scintillation counters to measure the timing of the positron.

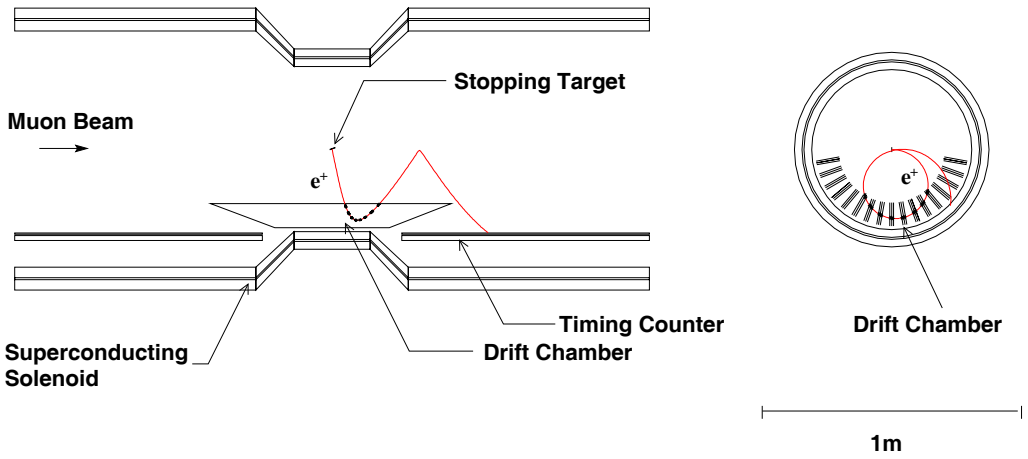

Figure 10: Schematic view of the positron spectrometer

Solenoidal magnetic field in general has a merit of confining low momentum tracks within a certain radius so that a large fraction of Michel positrons do not reach the track-detectors located at large radii. However, as shown in Fig.11(a), in a simple uniform solenoidal field such as the one adopted in the MEGA experiment, positrons emitted close to the 90° make many turns in the tracking chamber, thereby causing problems in pattern recognition or even making a stable operation of the chamber difficult. Also the bending radius of positrons of a given absolute momentum depend on the $\cos\theta$ angles, which makes it difficult to select high momentum tracks, as shown in Fig.11(b).

In order to avoid these problems, we adopt a solenoid with a gradient field, which provides the central field of 1.155 Tesla at $z = 0$ and slowly decreasing field as $|z|$ increases. As shown in Fig.12(a), the positrons emitted close to 90° are swept away by this gradient field much more quickly than in the case of the uniform magnetic field. This solves the first problem.

The gradient field is arranged such that monochromatic positrons from the target follow trajectories with a constant projected bending radius independent of the emission angle, as shown in Fig.12(b). That is, the bending radius is determined by the absolute momentum, and not by its transverse component. This allows us to sharply define the absolute momentum window of positrons to be detected by drift chamber cells.

Fig.13 shows the rate of Michel positrons per cm^2 per second as a function of radius for a muon decay rate of 1×10^8/sec. By placing the chamber at a radius larger than 20 cm the counting rate can be made very much below the limit of stable chamber operation. We note that the rates at outermost radii are especially low.

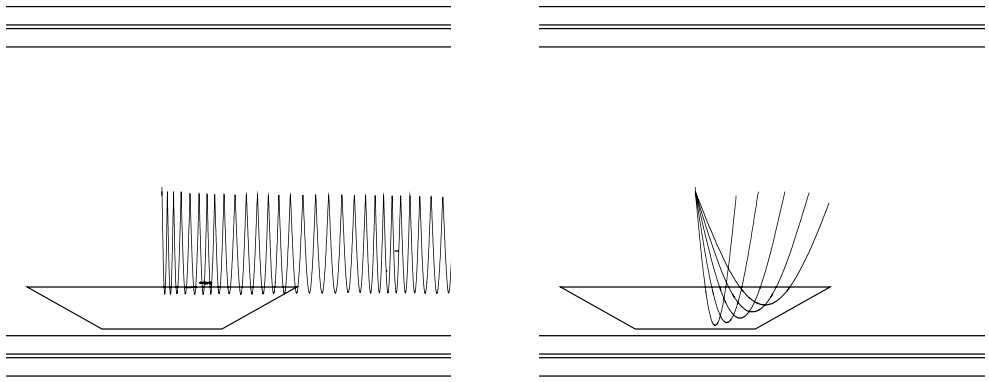

Figure 11: Problems with a uniform solenoidal magnetic field:
(a) $r - z$ view of the solenoid shown with the trajectory of a particle emitted at 88° making many turns inside the detector.
(b) Trajectories of monochromatic particles emitted at various angles. The bending radius depends on the emission angle.

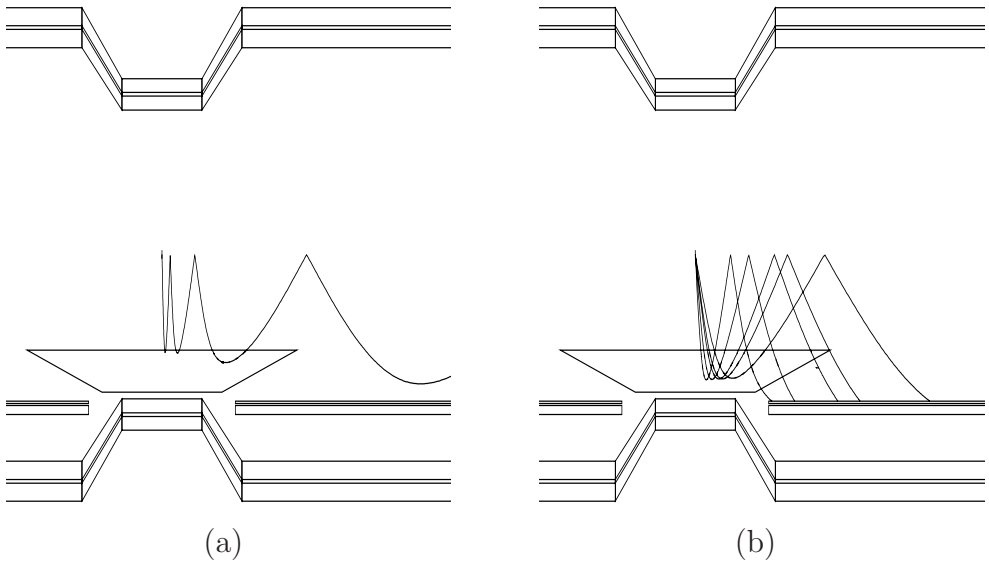

Figure 12: Advantages of a gradient magnetic field:
(a) $r - z$ view of the COBRA spectrometer shown with the trajectory of a particle emitted at 88°. The particle is swept away much more quickly than in Fig.11(a).
(b) Trajectories of monochromatic particles emitted at various angles. The bending radius is constant independent of the emission angle.

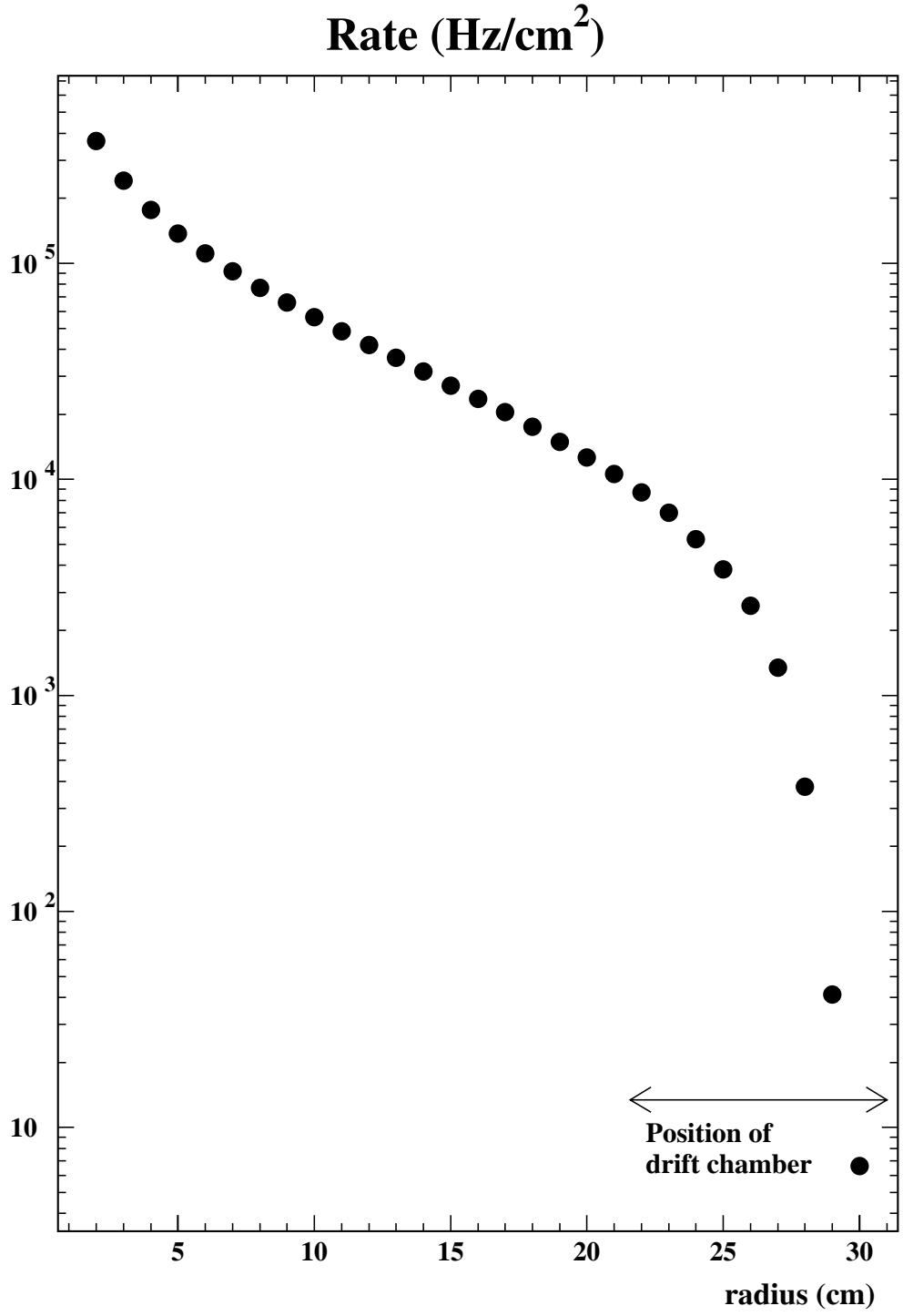

Figure 13: Rate of Michel positrons per cm^2 per second as a function of radius assuming a muon decay rate of 1×10^8/sec.

3.2.2 Thin-wall Superconducting Magnet

Superconducting solenoids with thin coils are commonly used in many particle physics experiments in these days. An example is the magnet onboard BESS [19] (Balloon-borne Experiment with Superconducting magnet Spectrometer), having a coil diameter of 1 m, and a length of 1.3 m, capable to produce 1.2 Tesla field [21]. The coil thickness including the cryostat walls is 4 g/cm^2 mainly in aluminum.

The magnet was constructed in 1990 and had experienced six annual balloon flights from 1993 to 1998. The magnet was transported to Canada and launched with full charged current every time. The flights continued typically for 24 hours at altitude of 37km, and ended with parachute-landing. The magnet experienced typically 40G landing shock on every impact. We never had any serious problem with this magnet during the entire operations. The twin magnet of this had also flown for 20 days around the south pole.

Based on these experiences, we have been developing a thinner coil with 2.7 g/cm^2 of material, which corresponds to 0.045 conversion length for 52.8 MeV γ rays of our interest. An expert in our collaboration, who designed and supervised the construction of many magnets including the ones mentioned above, is confident with the basic design of COBRA magnet with this thin coil, and has started detailed design work.

3.2.3 Chamber System

Present design of tracking detector is explained in the following. Other options are also under study.

Tracks are measured with 17 drift chamber sectors aligned radially at 10° intervals in azimuthal angle. Each sector consists of two staggered arrays of drift cells, as shown in Fig.14.

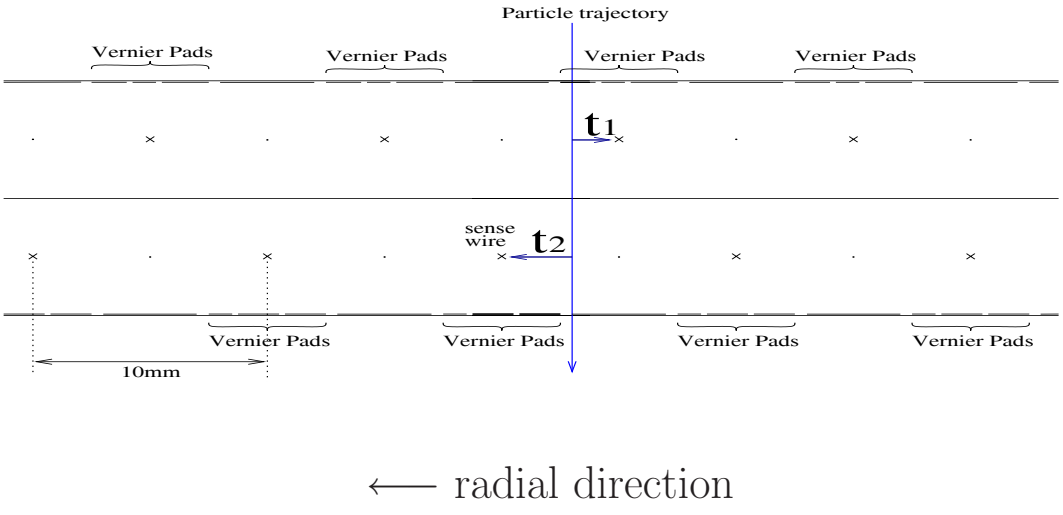

Figure 14: Cross-sectional view of a part of a chamber sector. It consists of two layers of drift cells staggered by half-cell.

The sensitive area of the chamber extends from a radius of 21.5cm to 31.0cm. In the z direction the active region extends up to $z = \pm 50$cm at the innermost radius and $z = \pm 22$cm

at the outermost. Positrons of 52.8 MeV/c emitted from the target with $|\cos\theta| < 0.35$ and $-60^\circ < \phi < 60^\circ$ are covered by this geometry.

This staggered-cell configuration allows us to measure the r-coordinate and the absolute time of the track simultaneously. Difference between the drift times $(t_1 - t_2)$ in the adjacent cells gives the r-coordinate of the track with $\sim$200 μm accuracy, while the mean time $(t_1 + t_2)/2$ gives the absolute time of the track with $\sim$5 nsec accuracy. This should work also for inclined tracks if the inclination can finally be obtained after iteration of the track fitting using also the hits on other sectors. We consider that this excellent time resolution is crucial, since accidental tracks of Michel decays can be rejected by offline analysis, if the pattern recognition and the track fitting are not disrupted too much.

By the ratio of charges observed at both ends of a sense wire the z-coordinate along the wire can be located first with an accuracy of $\sim$ 1 cm. The chamber walls are made of thin plastic foils. Thin layer of aluminum deposit on the foils is shaped to make a vernier pattern as shown in Fig.15. The ratios of charges induced on the three pads determine [22] the z position with an accuracy of 300 μm.

We plan to read each of the sense wire and the three pads with a Flash ADC. As shown in Fig.15, each hit then carries unambiguous three-dimensional information arriving at the same time. The system automatically has a multi-hit capability with minimum two-track resolution of about 1mm. we already have a lot of experiences on the 30 MHz flash ADC system to read 900 channels of BESS drift chambers and are starting to design 150 and 300 MHz systems by using the FADC chips from Signal Processing Technologies, Inc.

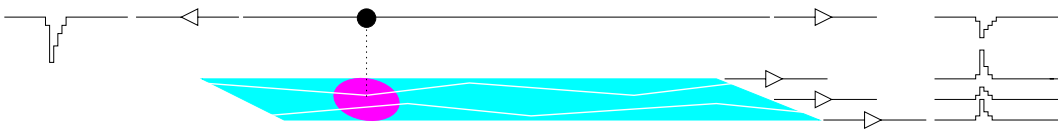

Figure 15: Charges induced on three vernier pads by an electron avalanche on the sense wire. From the ratios between the induced charges the hit position along the wire can be determined accurately.

The chamber sectors and the volumes between them are filled with 50% helium – 50% ethane gas mixture at 1 atm. The reason to choose the He based gas is to minimize multiple coulomb scattering of tracks. The mixture of He and C_2H_6 is known to work well in several existing experiments like BELLE [23] and BaBar [24]. A mixture of 50% He and 50% C_2H_6 has a long radiation length ($\sim$ 650 m) while the large ethane component gives sufficient ionization loss in the gas. The drift velocity saturates at roughly 4 cm/μsec for a relatively low electric field ($\sim$1.5 kV/cm) [25].

Figures 16 and 17 show the results of calculations using the GARFIELD program [26].

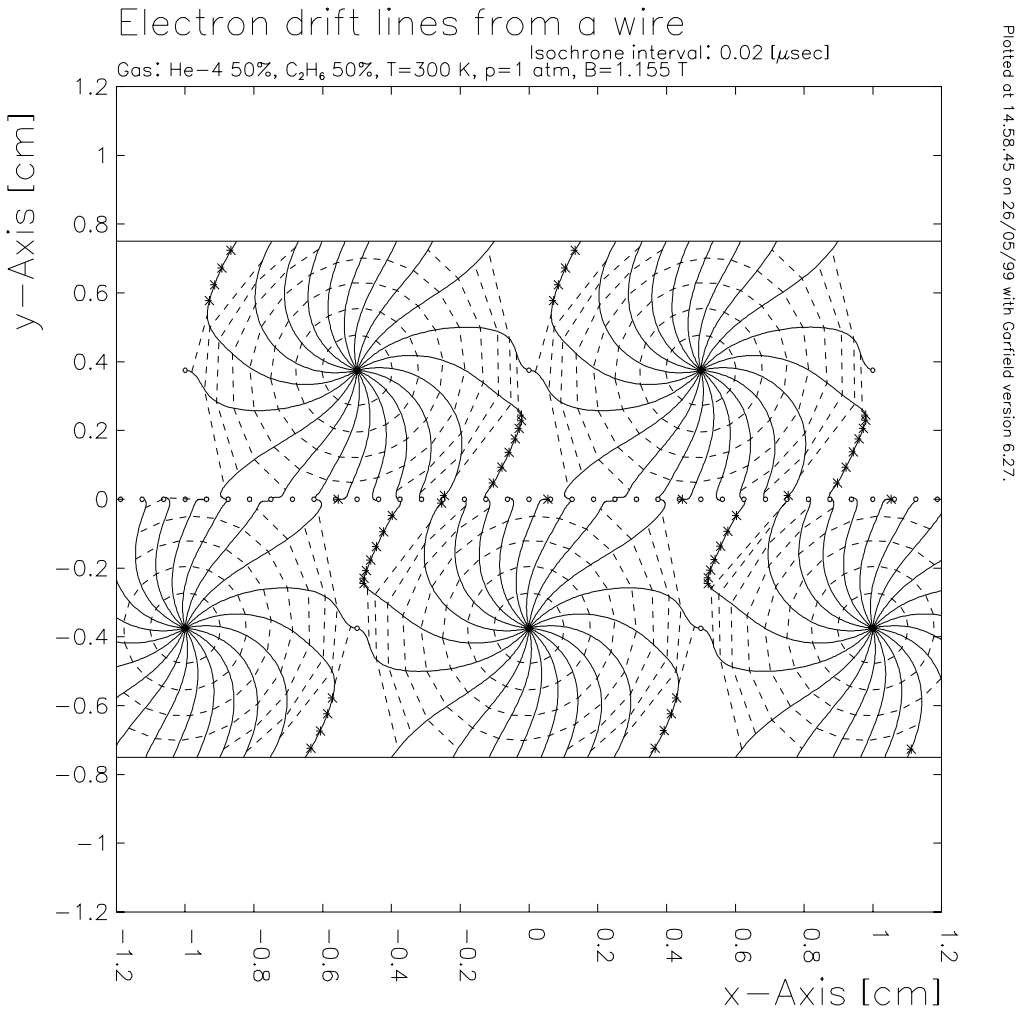

Figure 16: Drift lines of ionization electrons calculated with the GARFIELD program for a magnetic field of 1.155 Tesla. The three foils and the potential wire are at the ground potential. A positive high tension of 2000 volts is applied to sense wires. Note that the foil at the center is approximated in this calculation by an array of hypothetical wires.

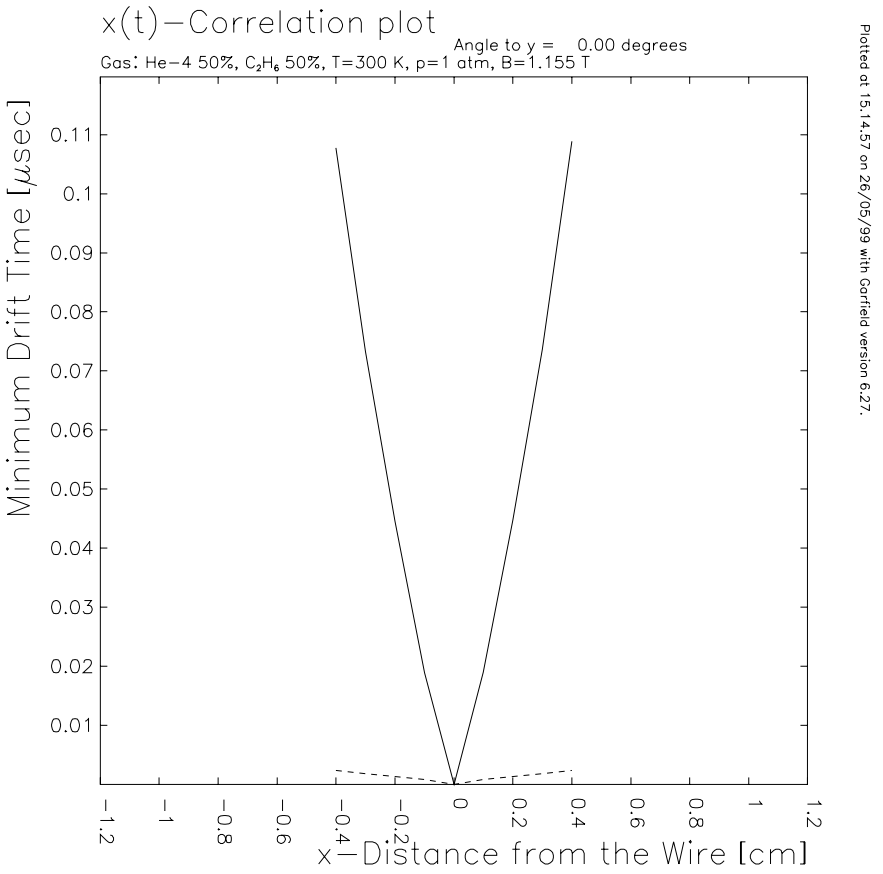

Figure 17: Relation between drift time and distance from the sense wire calculated with the GARFIELD program. The dashed line indicates the dispersion of the electron arrival time.

Even with the simple electrode configuration we expect a good enough position resolution. In the case of the BELLE central tracker a position resolution of $\sim 100\mu$m was obtained [23]. Momentum and angular resolutions are primarily limited by multiple scattering in the gas and chamber materials. Position resolution of chamber does not contribute much as long as it is less than 300 μm. A possibility of using 90% He and 10% C_2H_6 is also being considered to reduce the multiple scattering further while keeping the position resolution within an acceptable range.

To select the material for the chamber walls we are testing various plastic foils with thickness ranging from 2.5 μm to 12.5 μm. Kapton foil of 7.5 μm thickness is promising in view of strength, glueing and possibility of aluminum deposition. Fig.18 shows the structure of a chamber sector. In the present design a foil is stretched between two end-plates, which will be honey-comb structures made of thin plates of plastics and G10. An array of sense and potential wires are also strung between the end-plates. These end-plates are fixed to an aluminum plate of a cylindrical shape, which is then fixed to the inner wall of the magnet cryostat.

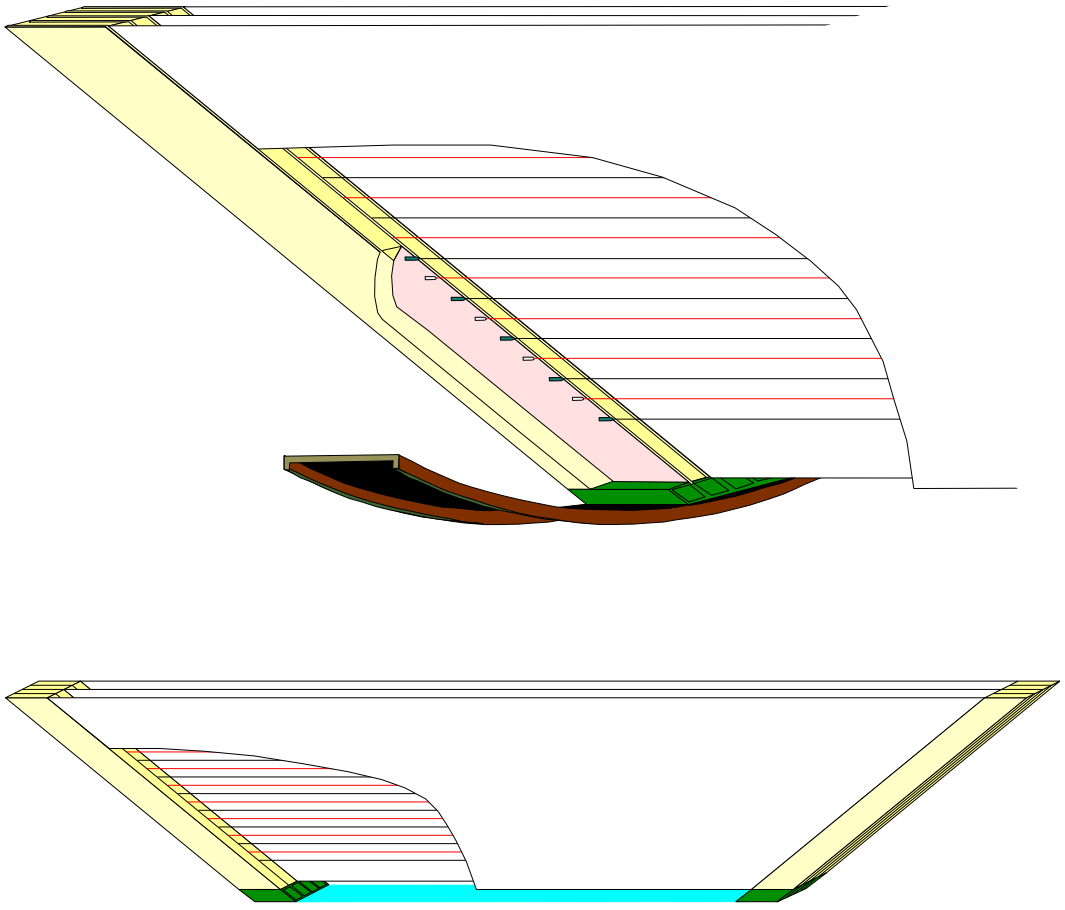

Figure 18: A sector of the drift chamber seen from the side. The end-plates stretching wires and foils are schematically shown.

3.2.4 Pattern Recognition

Fig.19 and 20 show examples of simulated $\mu \rightarrow e\gamma$ events with accidentally overlapping Michel decays occurring at an average of 1×10^8/sec.

With our constant-radius spectrometer most of low energy Michel positrons curl with small bending radii, and do not touch the drift chamber cells. Hit rates in outer drift cells are particularly low, as shown in Fig.13. Highest momentum positrons reach the outer drift cells, where the direction of the trajectories is almost perpendicular to the drift direction. A simple sum of the drift times $(t_1 + t_2)$ measured by the staggered cells then determines the absolute timing of the positron within 5 nsec.

A strategy of the offline reconstruction of tracks can be the following. We start from the hits in outer cells by picking up pairs of hits in adjacent staggered cells with the sum of the drift times close to the maximum drift time. Most of hits produced by accidental tracks are off timing and thus will fail to satisfy this condition.

The hits surrounded by circles in the figures are those satisfying this timing condition. It is found that the 52.8 MeV/c track of the positron from $\mu^+ \rightarrow \mathrm{e}^+\gamma$ always results in three or four sectors having a pair of hits satisfying the condition, while it is rarely the case for accidental tracks. We start from these hits and extrapolate the track toward smaller radii.

In the extrapolation process some hits at inner radii might be unusable by overlap of accidental hits. Simulation studies have shown that more than 90% of tracks have only zero or one hit lost by the overlap.

Probability of picking up wrong hits at inner radii is found to be small, since each hit-point carries the 3-dimensional information which is especially accurate in the z direction, namely 300 μm compared with the 1 m span of the sense wire. Lower figures of Fig.19 and 20 show the events in $x - z$ view, i.e. seen from the top of the detector. It is evident that individual tracks can be identified with the 3-dimensional information.

From these studies we are confident that the pattern recognition of the track will work at the muon decay rate of 1×10^8/sec. Studies are continuing to investigate if we can cope with a higher rate.

Present design of the chamber layout and the pattern recognition procedure will allow us to cover about 10% of the highest momentum window. This should be enough to determine the momentum resolution function from the real data.

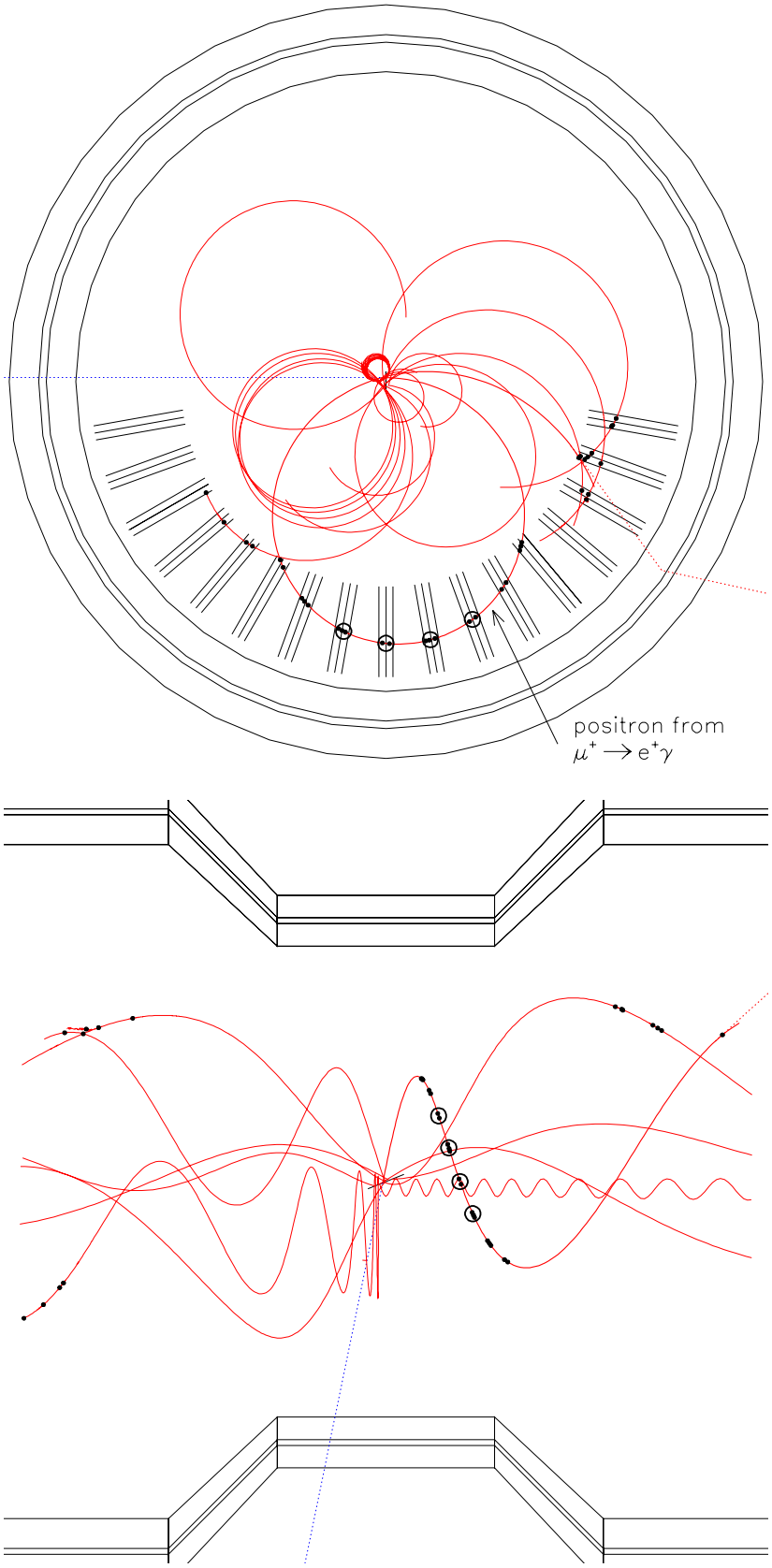

Figure 19: The $r-\phi$ view (upper figure) and the top view (lower figure) of a typical simulated $\mu^+ \rightarrow e^+\gamma$ event with accidental pile-up of Michel positrons. The positron from the $\mu^+ \rightarrow e^+\gamma$ is seen as the track with a large radius at the bottom of the $r-\phi$ view. Points within a circle are a pair of hits in adjacent staggered cells which satisfy the timing condition, as explained in the text, and are used as a starting point of pattern recognition.

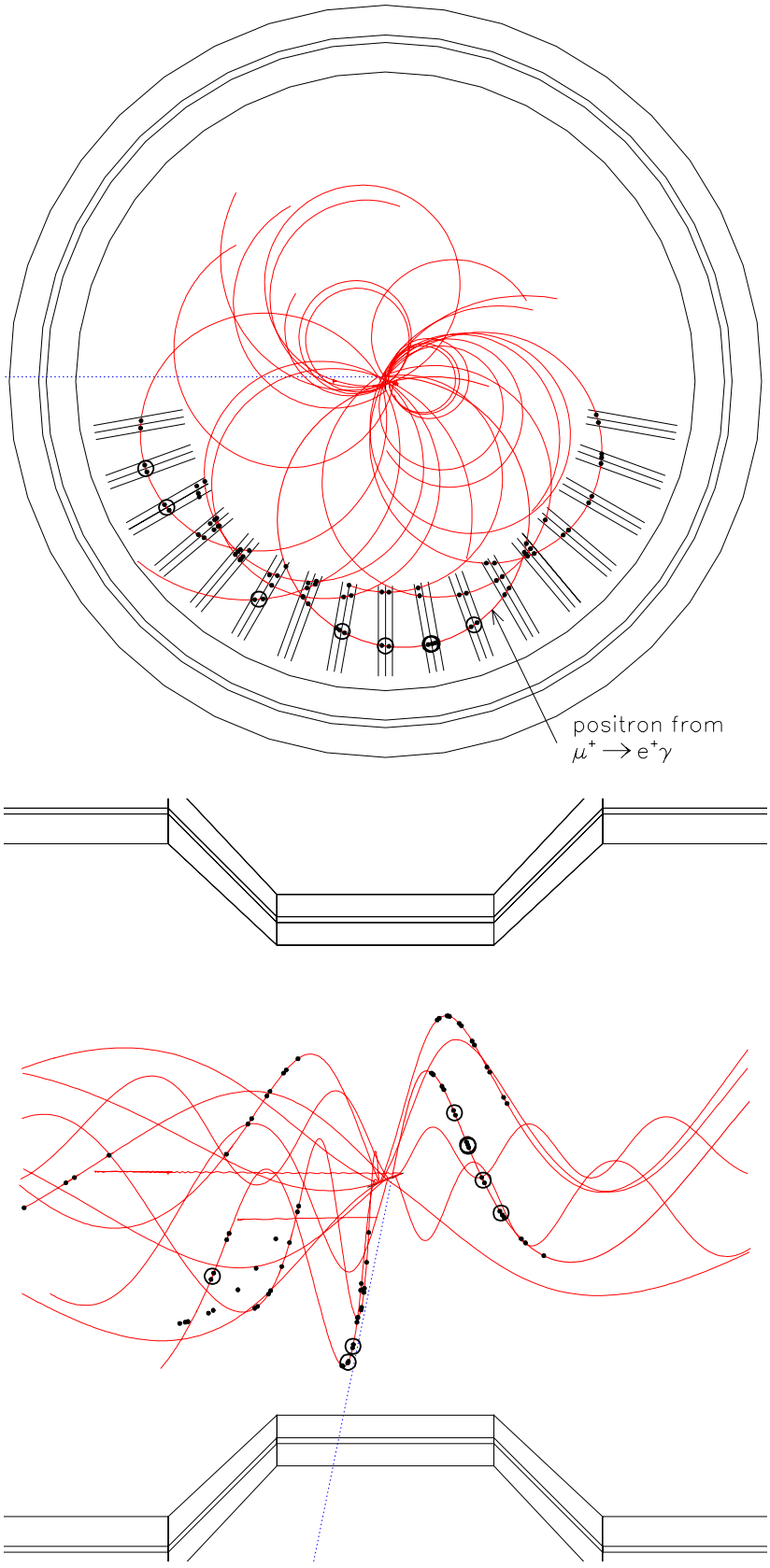

Figure 20: The $r - \phi$ view (upper figure) and the top view (lower figure) of a simulated $\mu^+ \rightarrow e^+\gamma$ event with accidental pile-up of Michel positrons. Individual tracks can be clearly identified with the 3-dimensional information carried by each hit-point.

3.2.5 Resolutions

Momentum and angular resolutions of the spectrometer are limited by multiple scatterings in the gas and the chamber material. As explained in 3.1, the central region inside the magnet is filled with pure helium (see Fig.22 in section 3.2.6) in order to minimize the amount of material in front of the tracking chamber as small as possible.

The expected resolutions of the spectrometer have been studied with GEANT simulations by incorporating detailed material distributions. Positrons of 52.8 MeV/c were generated and a simple circle fitting method was applied. The distributions of reconstructed momenta and emission angles are shown in Fig.21. The momentum resolution of 0.7% (in FWHM) and the angular resolution of 9 mrad (in FWHM) have been obtained. The momentum resolution is comparable with the MEGA design value. The angular resolution should improve by applying a fitting procedure similar to the Billoir method [27].

We are developing a full track fitting program combined with the pattern recognition procedure explained before in order to examine the effect of accidental hits on the resolutions.

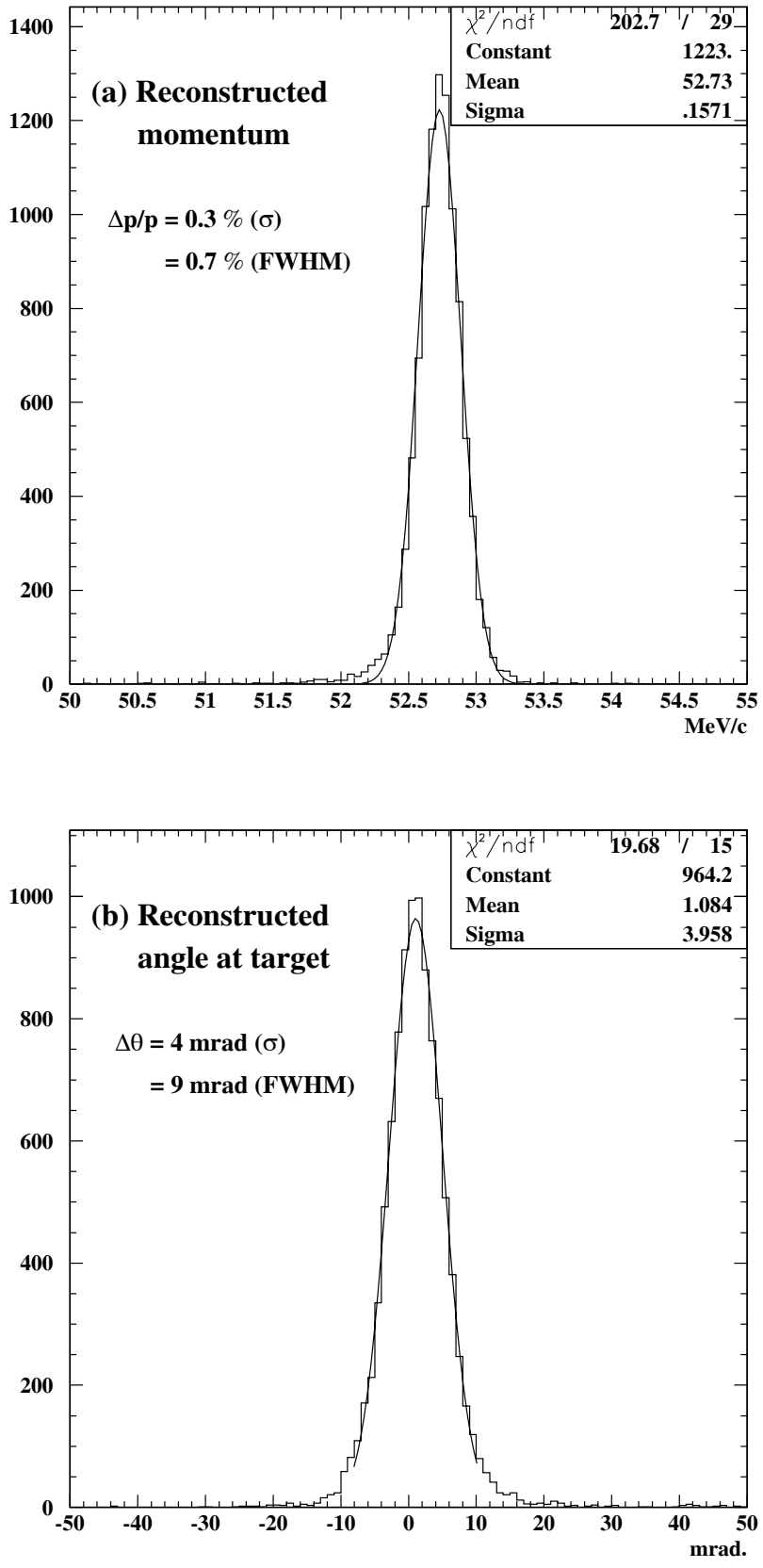

Figure 21: Distribution of momentum and angular resolutions. The events in the lower tail in (a) are caused by photon radiation from the positron.

3.2.6 Positron Timing Counter

Hodoscope arrays of plastic scintillators are placed on both sides of the positron spectrometer to measure the timing of the positrons and to provide the positron trigger signal.

Fig. 22 shows the present design of the layout. The timing counter arrays are placed at a radius of 33 cm, covering 120° in ϕ and longitudinal position of $27< |z| < 125$ cm. The $\mu \rightarrow$ e γ positrons emitted in the angular range $|\cos\theta| = 0.08$ to 0.35 are incident on the timing counter after turning 1.5 circles in r-ϕ plane.

The effect of the multiple scattering to the timing measurement is evaluated by a full simulation which incorporates detailed material distributions. Fig. 23 shows the resultant plot of t (the impact time of positrons on the timing counter) vs. z (the z-coordinate of the impact point). The multiple scattering causes a spread of typically ± 2 cm on z, which would correspond to a timing spread of ± 50 psec. However the t and z are very much correlated to each other, and a measurement of z at an accuracy of ± 1 cm will reduce the time spread to ± 20 psec, as shown in Fig. 24. Therefore the effect of the multiple scattering is negligibly small as compared to the detector resolution.

Fig. 25 shows the configuration of the timing counter, which consists of two layers of scintillator hodoscopes, orthogonally placed along ϕ and z directions, respectively. The scintillators which compose each layer can have a slant shape, so that a positron incident to the hodoscope crosses two or three adjacent scintillators. The pulse-height ratios among these adjacent scintillators will provide an information on the impact point with accuracy better than ± 1 cm for z and ± 3 cm for ϕ directions. Each scintillator is viewed from both ends by two photomultipliers, which measure the pulse heights as well as the arrival times of the scintillation light (t_L and t_R) at both ends. The time difference $t_L - t_R$ provide another measurement of the impact point along the scintillator (ϕ for the inner and z for outer scintillators), while the mean time $(t_L + t_R)/2$ measure the absolute impact time. Thus we have redundant and independent measurements both for the timing and for each coordinate of the impact point.

We note that any error in the above procedure of the timing determination, such as the disruption of z-measurement by an accidental hit, might result in a small inefficiency of the signal, but not to the enhancement of the accidental background, which would ultimately limit our sensitivity.

In order to estimate the accidental hit rate of the scintillators, Michel decay positrons are generated and followed to the timing counters by GEANT simulation, which shows that 2% of Michel decays are incident to the timing counter at each side. This corresponds to an average counting rate per scintillator of 0.1 MHz, resulting to an occupancy of 10^{-3} for a time window of 10 nsec.

The momentum window for the Michel decay is reasonably flat between 47 to 52.8 MeV/c, which is wide enough to experimentally determine the resolution function of the spectrometer from the real data.

We envisage to use BC-404 from BICRON as the scintillator and the ultra-fine-mesh PMT of Hamamatsu, which can be operated in a strong magnetic field. The TOF system of BELLE experiment [23] with 4 m long scintillators is achieving 50 psec rms resolution in 1.5 Tesla field and in a high rate environment. We have our own experiences with BESS experiment [19] of maintaining overall 51 psec rms (Fig. 26) for cosmic rays incident from various directions with 0.95 m long scintillators covering an area of 1 m^2 in 0.3 Tesla stray field. Extrapolations from

these experiences allow us to conclude that a timing resolution better than 100 psec FWHM can be obtained with the present design of the timing counter. We have all electronics (fast discriminator and TDC with 25 ps/ch resolution etc.) which were developed for BESS and are necessary to achieve this timing resolution.

Prototype construction of the scintillator array has started, in order to confirm the timing resolution and to optimize the design.

The measurement of the impact point at the timing counter will also provide an important check of the momentum and angle measurements by the spectrometer, since real high-momentum positron must follow the extrapolated track and arrive at the timing counter within a few cm of the expected impact point, while this will not be the case if the pattern recognition or the track fitting is disrupted by some reason such as the pile-up tracks or the accidental hits in the drift chamber.

With present design we have an option of placing a thin drift or MWPC chamber, if more accurate determination of the incident point become necessary, although we do not believe this to be the case.

Photomultipliers have a limited life time in the helium gas. As shown in Fig. 22, the area surrounding the timing counters are separated by two layers of metal-coated plastic films from the central region which is filled by helium gas. N_2 gas flows in between the plastic films and in the area containing timing counter. Such system is known to assure a long-enough life time of PMTs.

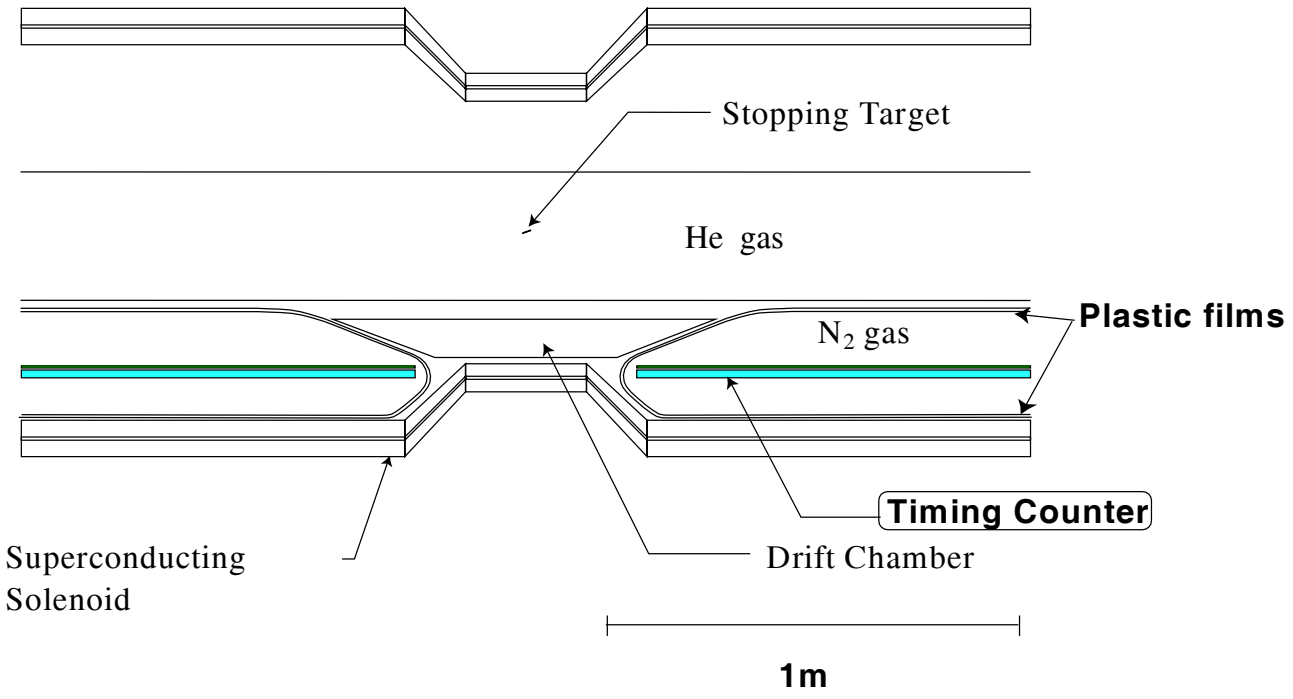

Figure 22: The present layout of positron timing counters

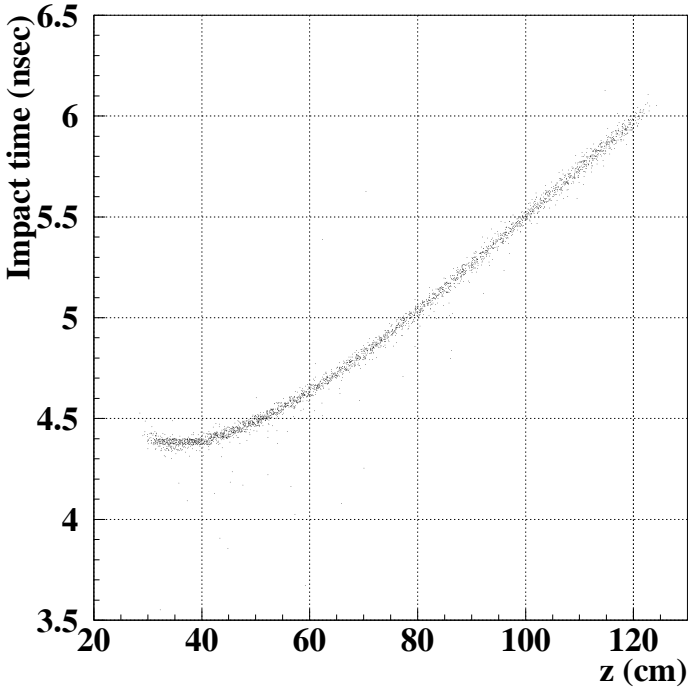

Figure 23: The correlation between the impact-time t (nsec) and the z-coordinate of the impact point(Simulation). The positrons from $\mu \rightarrow$ e γ are generated in the range $|\cos\theta|$=0.08$\sim$0.35. The line spread is due to the multiple scattering.

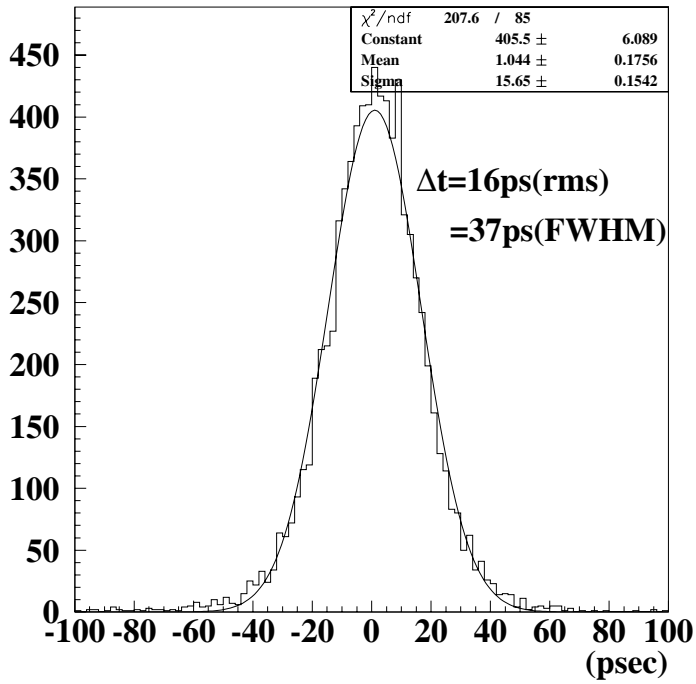

Figure 24: The spread of the positron timing caused by the multiple scattering.

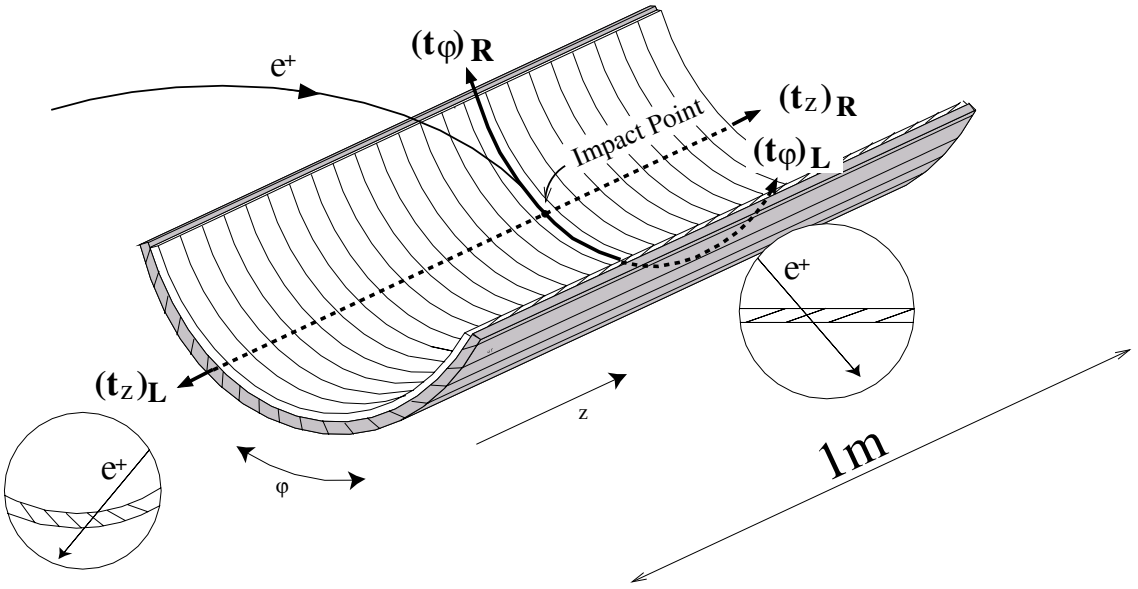

Figure 25: The configuration of the timing counter

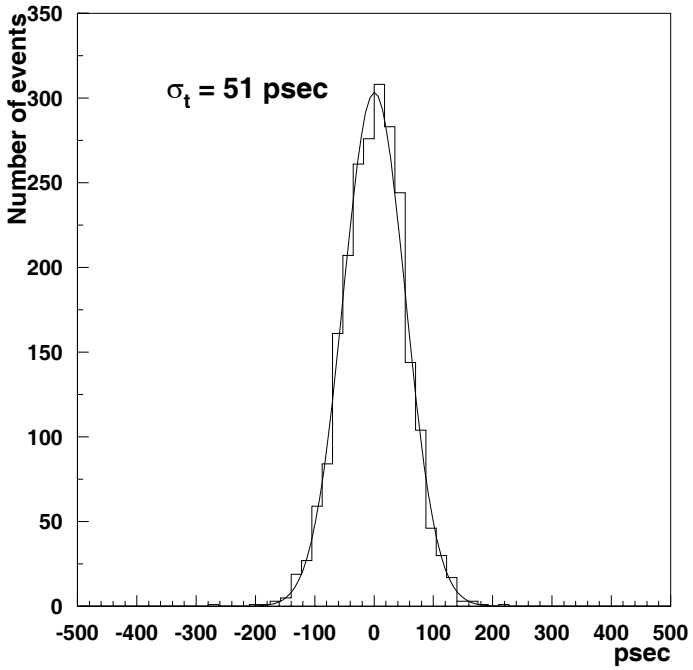

Figure 26: Overall timing resolution obtained [20] with the hodoscope array onboard BESS spectrometer. The plots are for high energy cosmic-ray protons collected during a balloon flight. The hodoscope consists of 12 scintillators, each with dimensions of 95 cm length, 10 cm width and 2 cm thickness, viewed from each end by a photomultiplier (HAMAMATSU R6504S) placed in 3 kG stray magnetic field. Experiences indicate that the timing resolution will improve for scintillators with smaller widths.

3.3 Photon Detector

We use only the scintillation light from liquid Xe, and do not attempt to collect ionizations. This makes the construction and operation of our photon detector very much simpler. Liquid Xe scintillator has high light yield (75% of NaI(Tl)) and fast signals (Fig. 27), which are the most essential ingredients for precise energy and timing resolutions required for this experiment. Its short decay-time is indispensable to minimizing pile-up of high rate γ rays. Liquid Xe is also free from a problem of non-uniformity, which limits the energy resolutions of scintillating crystals.

Properties of liquid Xe are summarized in Table 2.

Table 2: Properties of Liquid Xe

Density	3.00 g/cm^3
Boiling and melting points	165 K, 161 K
Energy per scintillation photon	24 eV [28]
Radiation length	2.77 cm
Decay-time	4.2 nsec, 22 nsec
	45 nsec (75%) [29]
Scintillation light wave length	175 nm
Scintillation absorption length	$>$ 100 cm
Attenuation length (Rayleigh scattering)	30 cm
Refractive index	1.57

A design of the liquid Xe photon detector is shown in Fig. 28.

We adopt here a simple "mini-Kamiokande" scheme [30], i.e. a liquid Xe volume (0.8 m^3) is viewed from all sides by arrays of 800 photomultiplier tubes (PMTs). With an effective coverage with the photocathode of PMTs reaching $\approx$ 35 %, a high photo-electron statistics necessary for a 1% level energy resolution is assured. The outputs of these 800 PMTs provide detailed image of the scintillation to measure the position of the photon-conversion and to identify pile-up γ rays. High precision ADCs are used for an accurate determination of γ energy. TDC information from all 800 PMTs will result in an excellent timing resolution for the γ rays. In addition every PMT will be read by a fast flash ADC of 150 or 300 MHz, thereby allowing us to recognize the pile-up of accidental γ rays.

The detector is located outside the very thin magnet, that is 95 % transparent to a 52.8 MeV γ ray. It is shielded from the stray magnetic field by correction coils and iron structure. The surface of the liquid Xe is at 65 cm from the target center and its depth is 47 cm. The fiducial volume of the detector covers a solid angle of $\Delta\Omega/4\pi$ =12% ($|\cos\theta| < 0.35$ and 120° in ϕ).

The temperature of liquid Xe is –100°C, i.e. much higher than –200°C of liquid N_2. The thermal insulation and the cooling is thus rather easy and simple.

Engineering design of the cryostat for the liquid Xe detector is in progress (Fig. 29). It consists of the Xe vessel and vacuum vessel for thermal insulation. In its front face, a honeycomb structure made of aluminum is used to reduce materials for incident photons. A total thickness of honeycomb base-plates is about 6 mm (3mm each) for the Xe vessel, and less than 5 mm for the vacuum vessel. The whole cryostat is also made of aluminum.

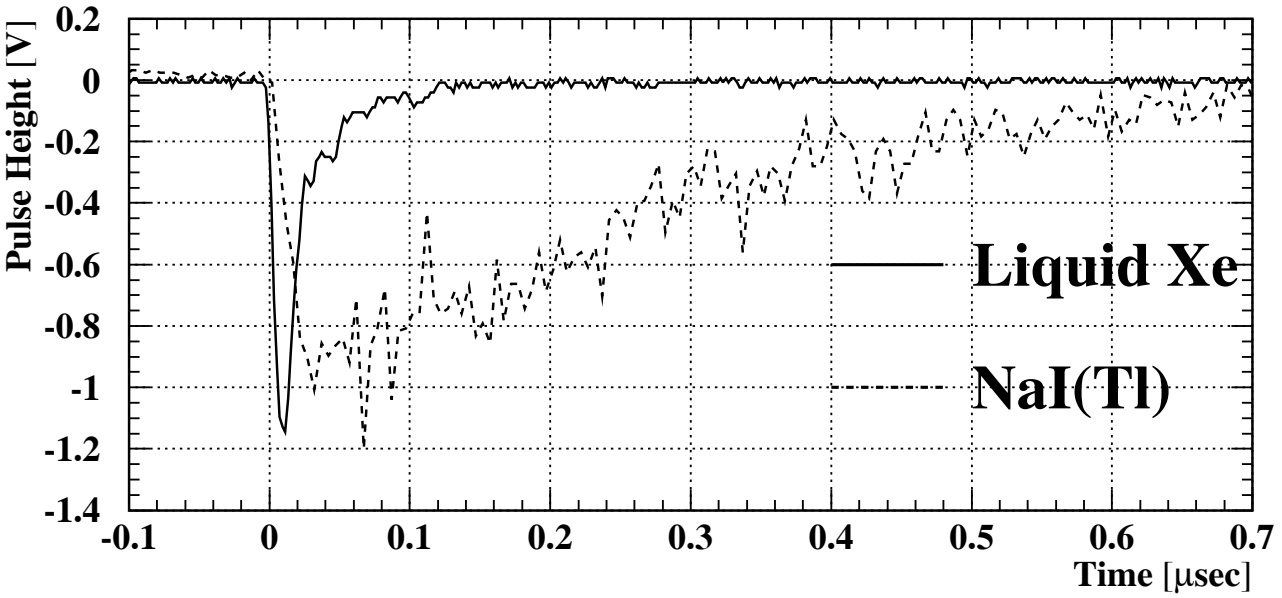

Figure 27: A typical liquid Xe signal from γ ray of 320 keV, superimposed with a NaI signal.

As a cooling system of liquid Xe, a direct-cooling refrigerator without coolant will be used. It has a cooling power of about 250 W whereas heat from the photomultiplier bases is 80 W in total. Liquid N_2 lines are also installed for initial cooling.

Bunches of thin cables for signal and HV are taken out through special feedthroughs developed for ATLAS [31]. The structure to support arrays of PMTs are installed through the side flange. The space between the PMTs is filled with plastic filler attached at the support structure to prevent liquid Xe to seep in.

Our experiences show that the required purity of liquid Xe is very modest for scintillation as compared to the case for ionization collections. However we shall take maximum caution: Xe is purified before being liquefied with a similar method as described in [32] where Xe gas is flushed through Oxisorb [33] cartridges and molecular sieves. During operation, Xe gas, evaporated from liquid Xe, will be recirculated through the purification system. The purity of the liquid will be monitored by ionization chambers.
The whole system is installed on a movable stage, which is used for mapping the whole detector through calibration by tagged photon beam (Sec. 3.3.3).

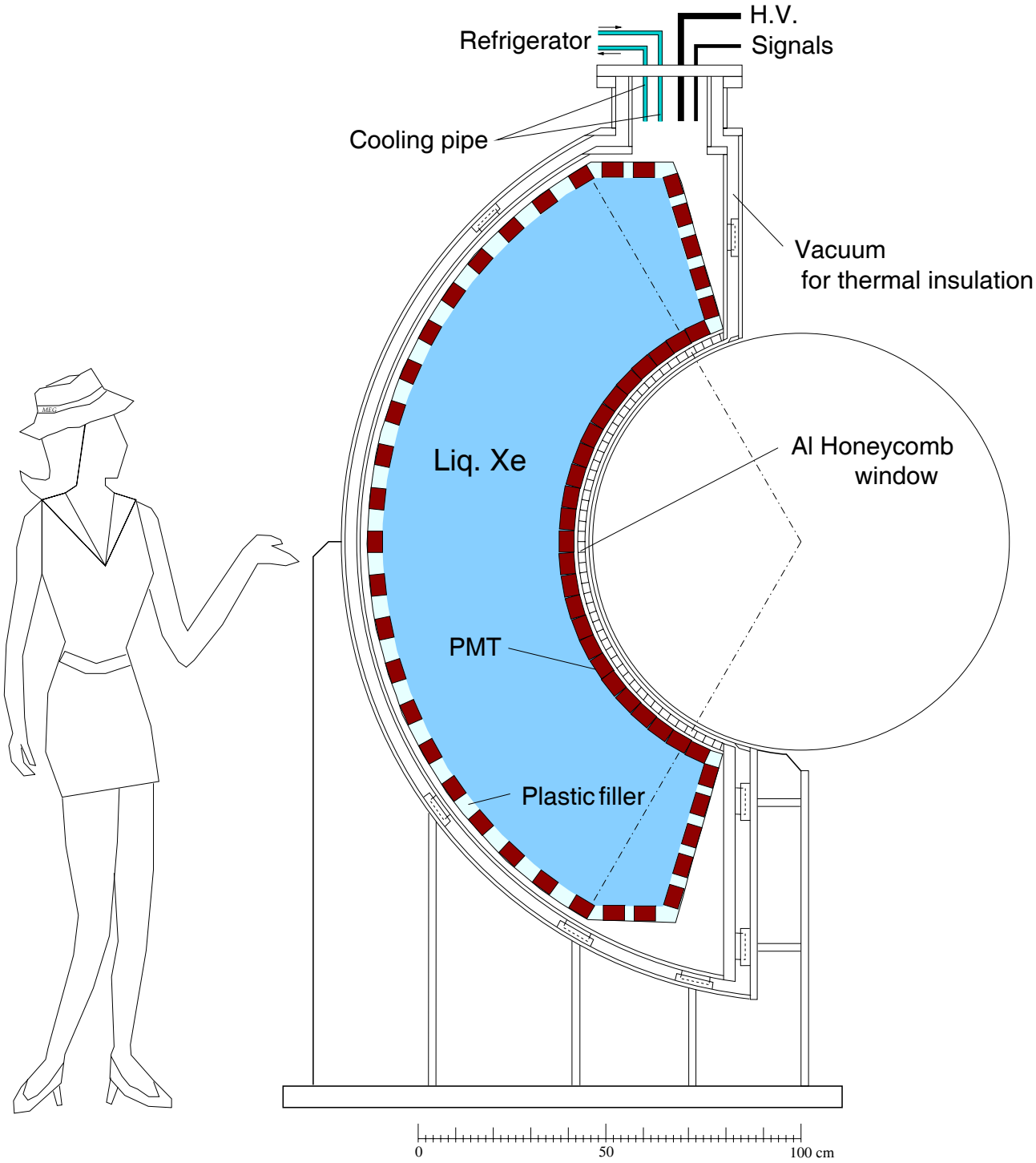

Figure 28: A cut view of the "mini-Kamiokande" detector.

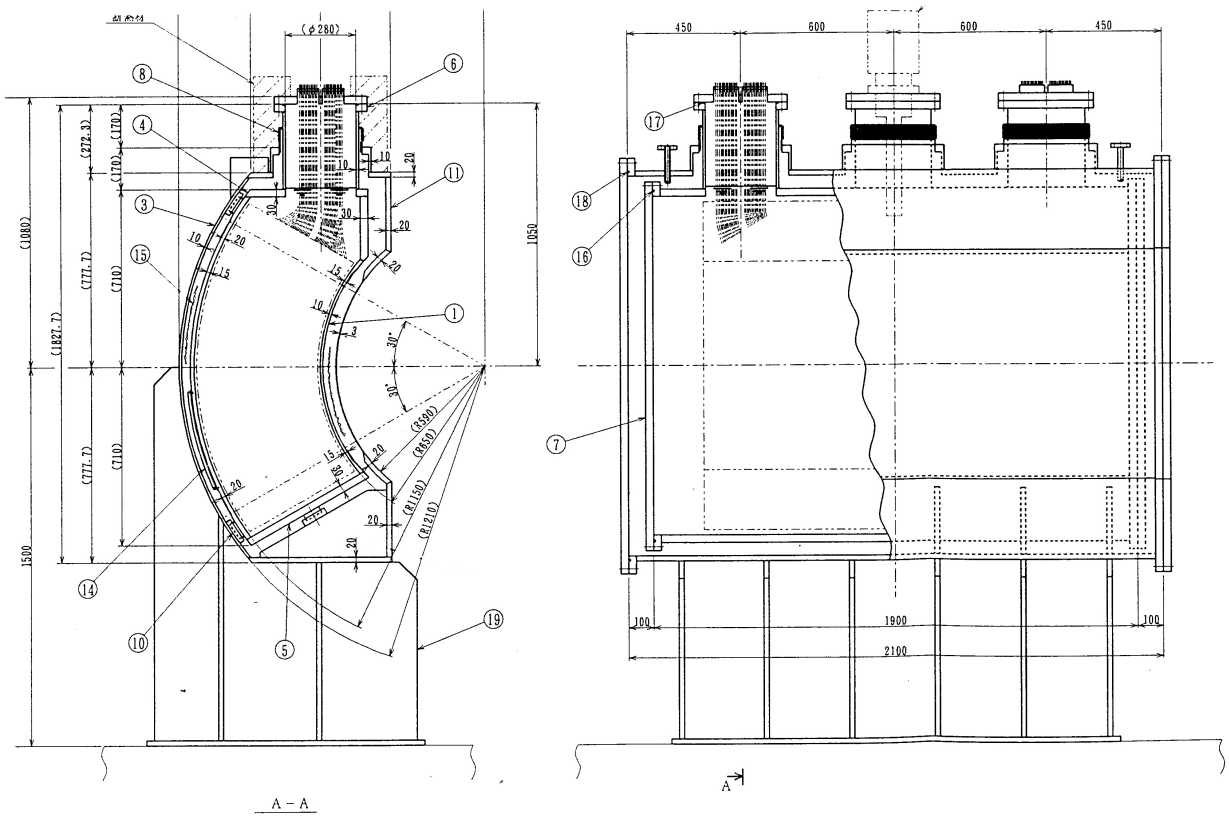

Figure 29: A preliminary engineering design for liquid Xe vessel.

3.3.1 Expected Performance

Detailed Monte Carlo simulations are performed to investigate the performance of the liquid Xe detector. The simulations are all based on the results obtained from our prototype detector (See Sec. 3.3.2). In this Section resolutions are all given in FWHM unless otherwise noted.

Position and Timing Measurement

A 50 MeV γ ray entering the liquid Xe loses most of its energy near the entry point, typically within 2–10 cm from the surface (Fig. 30), resulting in a distribution of the PMT outputs as shown in Fig. 31(a). In the simulation the 2" ϕ PMTs are placed at intervals of 6 cm. According to the simulation, the γ ray position, using the weighted mean of this distribution, can be determined to a precision of 4 mm (Fig. 31(b)), which corresponds to an angular resolution of $\Delta\theta_\gamma = 6.4$ mrad, given the 2.1 mm accuracy of the μ decay point determined by the positron spectrometer (Sec. 3.2.5).

When the γ conversion occurs within 1 cm from the plane of the PMT surface, much of the scintillation light concentrates on a single PMT or escapes through spaces between PMTs. Even in this case, using the tail of the light distribution, the γ incident position can be determined with a precision of 6.8 mm, corresponding to a 10 mrad error in θ_γ.

The distribution of the PMT outputs becomes broader when the γ ray conversion occurs deeper inside the Xe volume, as seen from Fig. 32. Using the broadness of the distribution, the depth of the γ ray conversion point (z_γ) can be determined with a precision of 16 mm (Fig. 33).

The accuracy of the conversion point determination is translated into a timing resolution of 50 psec. The front PMTs detect direct scintillation light from the same γ conversion simultaneously. With the fast rise time and the high scintillation light statistics, they will provide a timing determination with a resolution of 0.1 nsec. An R&D study to further improve this accuracy is currently under way.

Energy Measurement

Plotted in Fig. 34 is a total sum of all the PMT outputs for 52.8 MeV γ rays whose conversion points are identified as $z_\gamma > 2$ cm. No corrections for the conversion position are made. The sharp peak corresponds to a 1.4 % energy resolution.

The lower tail of the energy distribution is dominantly due to the energy leakage (back scattering of soft γ rays) from the Xe front surface. γ interactions in the materials between the target and the Xe (the PMTs and their support, the Xe vessel, and the magnet) also contribute. These front materials are 90 % transparent to a 52.8 MeV γ ray. It is noted that the tail does not degrade the energy resolution but only worsens the detection efficiency. Fig. 35 shows the detection efficiency of 52.8 MeV γ rays as a function of the γ energy cut. With ± 2 % energy cut, the detection efficiency is 73 %.

When the γ conversion occurs near the PMT surface ($z_\gamma < 2$ cm), the total sum of the PMT outputs becomes very sensitive to the position of the conversion point relative to the PMT alignment (Fig. 36). This can be avoided by excluding the front PMTs from the total sum. In this case, with a loss of scintillation light statistics, the energy resolution becomes slightly worsened to 2.0 %.

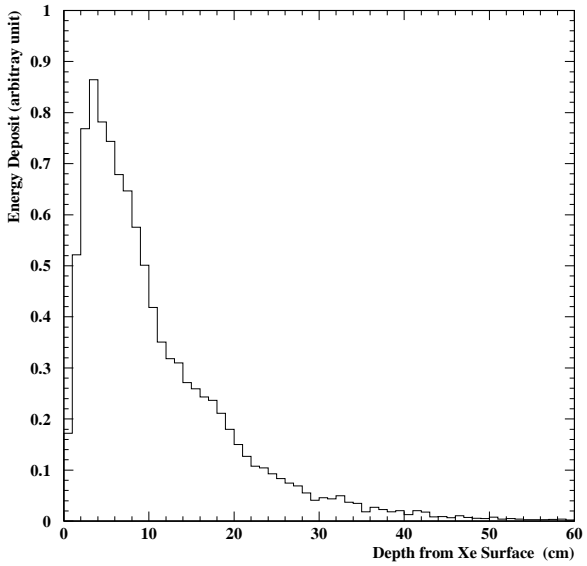

Figure 30: An average energy deposit as a function of the distance from the liquid Xe surface for a 52.8 MeV γ ray.

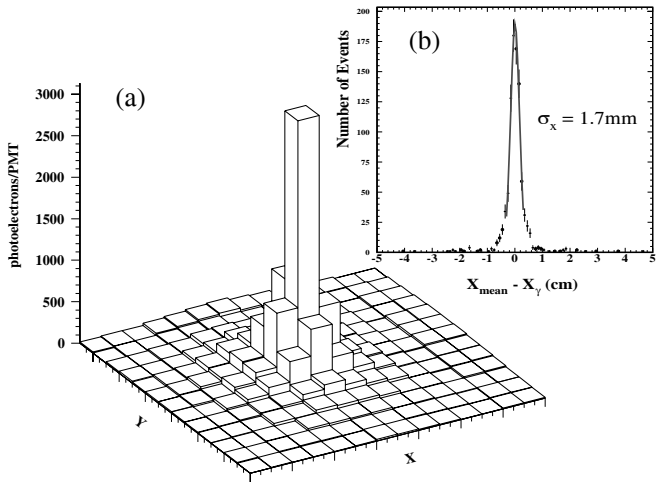

Figure 31: (a) A typical spatial distribution of light observed for a 52.8 MeV γ ray. Each bin corresponds to a 2"ϕ PMT output; (b) A spatial resolution obtained with weighted means.

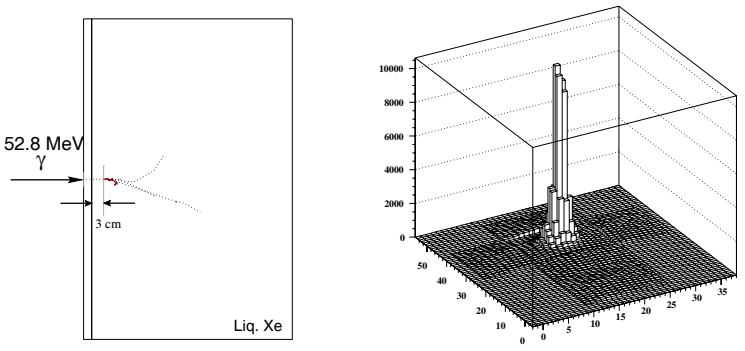

(a)

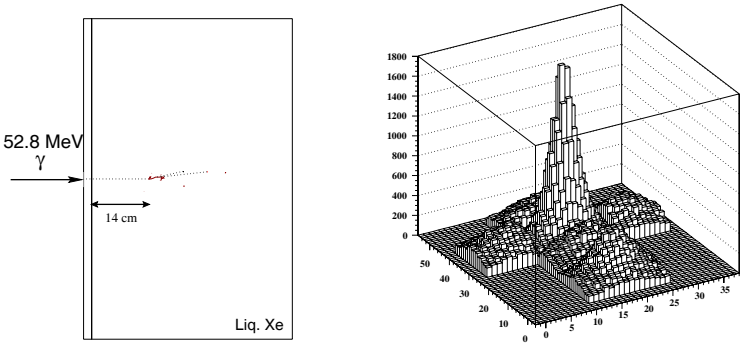

(b)

Figure 32: (a) A display of event where the γ ray converted at $z_\gamma = 3$ cm. The right plot shows the distribution of the PMT outputs. (b) An event with $z_\gamma = 14$ cm.

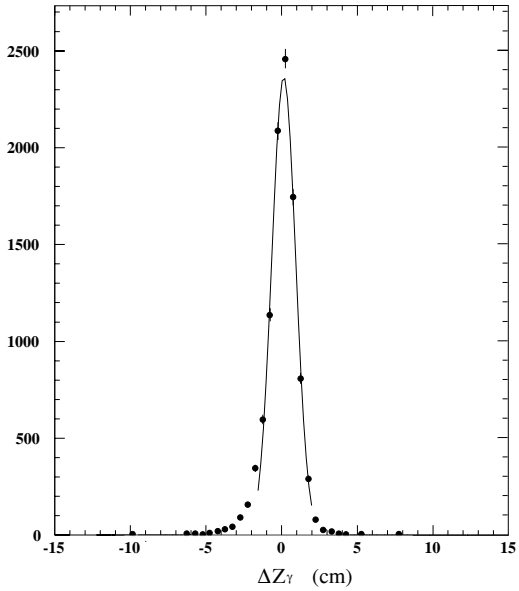

Figure 33: An obtained resolution of γ conversion point z_γ.

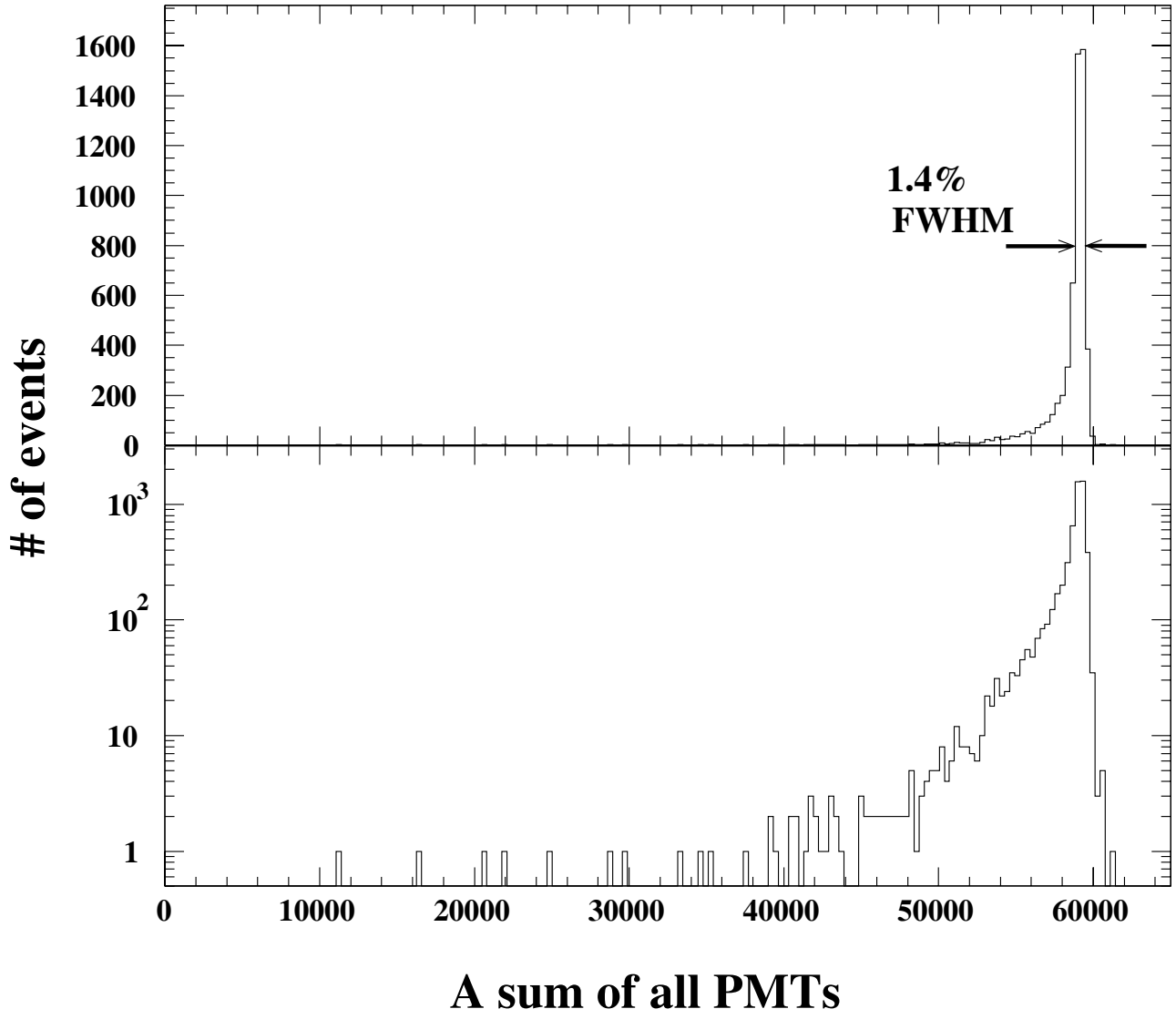

Figure 34: A sum of all PMT outputs (arbitrary unit) for 52.8 MeV γ ray identified as $z_\gamma > 2$ cm. (Bottom: same plot in logarithm.)

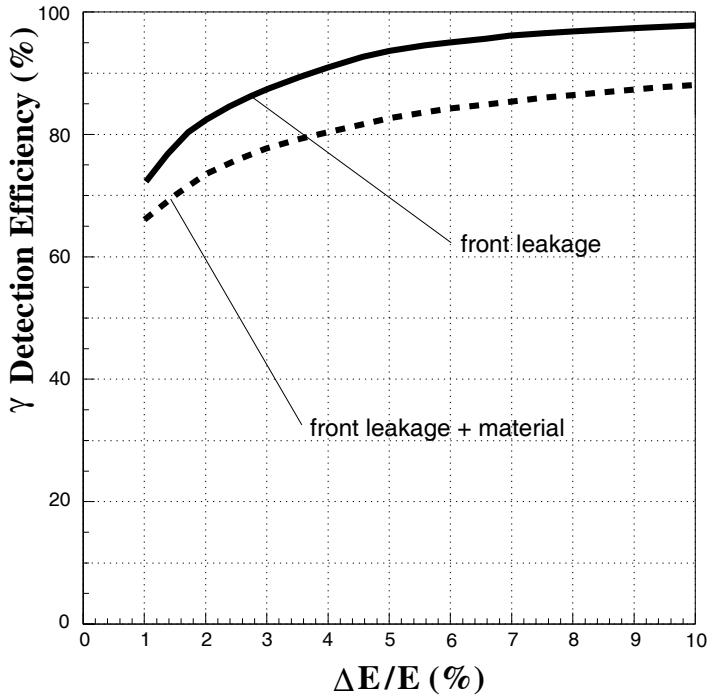

Figure 35: Detection efficiency of a 52.8 MeV γ ray as a function of half width of energy cut ($\pm\Delta E_\gamma$).

Pile-up of Multiple γ Rays

We make the best use of the scintillation image of γ interactions provided by the 800 PMTs and the fast pulse-shape of liquid Xe scintillation to minimize pile-up of γ rays which could increase background rates. Fig. 37 shows a simulation of a potential pile-up event. There are three handles to separate pile-up γ rays: spatial separation of two γ rays by the distribution of the PMT outputs (Fig. 37(c)), pulse timing of the pile-up γ ray by the PMT nearest to its conversion point (Fig. 37(b)), and pulse-shape separation of the PMT signals (Fig. 37(a)).

Densely placed PMTs effectively function as segmented cells (Fig. 37(c)). According to Monte Carlo simulations, two γ rays, each with an energy greater than 5 MeV, can be identified if their incident positions are separated by more than two PMTs (15 cm or 0.2 rad in angles).

Pulse-shape analysis further reduces pile-ups with lower energy photons using the outputs of the 150–300 MHz flash ADCs equipped to each PMT (Fig. 37(a)). A study with Monte Carlo simulations indicates that two γ rays, each with an energy greater than 2.5 MeV, can be reconstructed if their time difference is more than 10 nsec.

Effects of γ ray pile-ups on the background rates are addressed in Sec. 4.2.2.

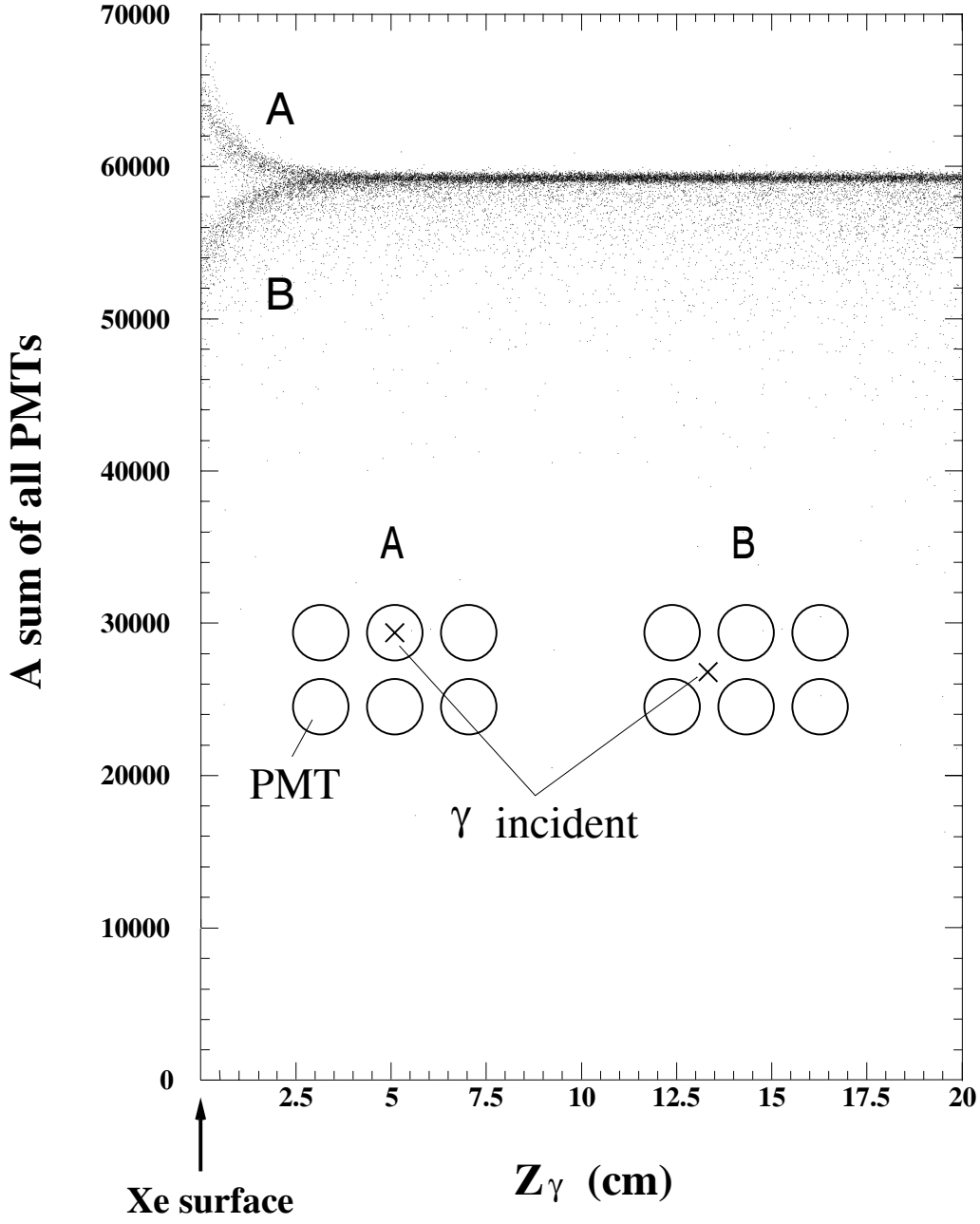

Figure 36: A sum of all the PMT outputs (arbitrary unit) vs. the depth of the γ conversion point (z_γ).

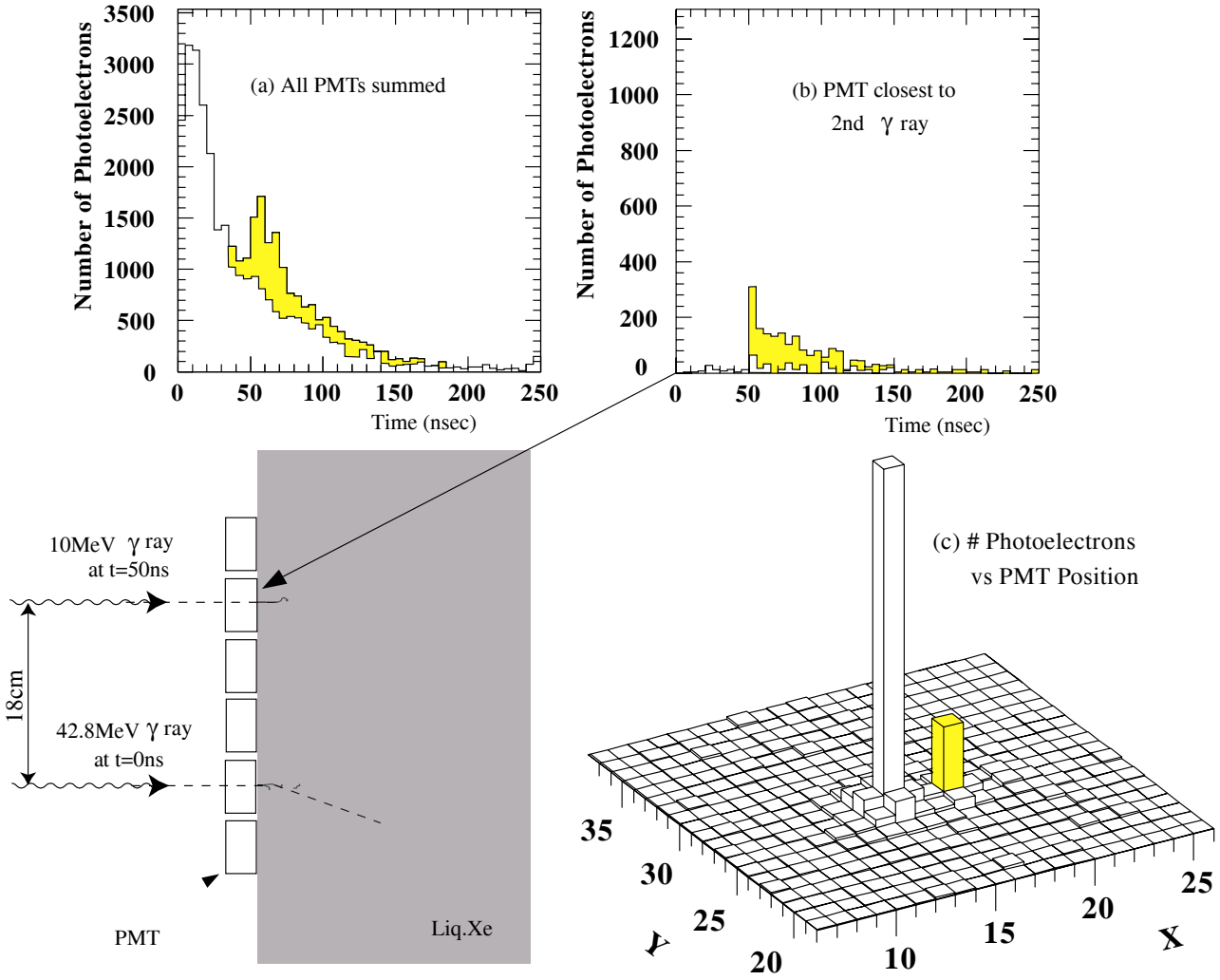

Figure 37: A simulated event in which a 43 MeV photon is followed after 50 ns by a 10 MeV photon. Open histograms correspond to signals of the 43 MeV photon and the shaded ones to those of the 10 MeV photon. (a) Pulse-shape (all PMTs summed); (b) Timing of the 10 MeV photon measured by the PMT closest to its conversion point; (c) Spatial separation by the distribution of the PMT outputs (each bin corresponds to a 2"ϕ PMT).

3.3.2 Prototype Construction and Tests

In order to be confident on the photon detector we propose the first prototype was quickly constructed, and various tests were performed.

The prototype has an active volume of $116 \times 116 \times 174$ mm^3 viewed by 32 UV-sensitive PMTs [34]. The PMT has a quartz window to transmit the ultra violet light, and can be stably operated at the liquid Xe temperature of –100°C. The properties of the PMT are summarized in Table 3. A schematic view of the detector is shown in Fig. 38. The detector was placed

Table 3: Properties of R6041Q.

PMT size	57 mmϕ
Photo-Cathode material	Rb-Cs-Sb
Size of effective area	46 mmϕ
Q.E. at normal temperature	10% – 15%
Dynode type	Metal channel
Number of stages	12
Typical H.V.	1000V
Current amplification	9×10^6

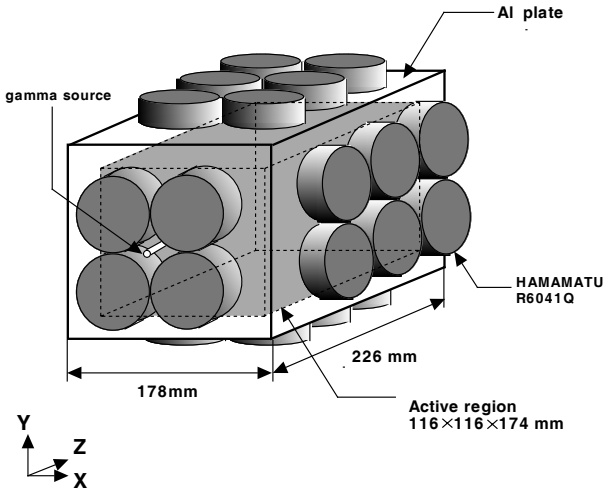

Figure 38: A schematic view of the first prototype photon detector

inside a large vessel which was filled with liquid Xe as shown in Fig. 39. In order to study the energy and position resolutions, several γ ray sources from 0.32 MeV to 1.8 MeV were located at one end of the detector as indicated in Fig. 38. An α source ^{241}Am was attached at the opposite end.

Fig. 40 shows time dependence of a typical PMT output from the α source as a function of the time immediately after the vessel was filled with liquid Xe. After the initial gain change of a few %, all 32 PMTs were found to be stable within $\pm0.5\%$ for many days.

Fig. 41 shows the energy resolution (rms) measured for γ rays from ^{51}Cr, ^{137}Cs, ^{54}Mn and ^{88}Y in comparison with the predictions of Monte Carlo simulation. The simulation utilizes

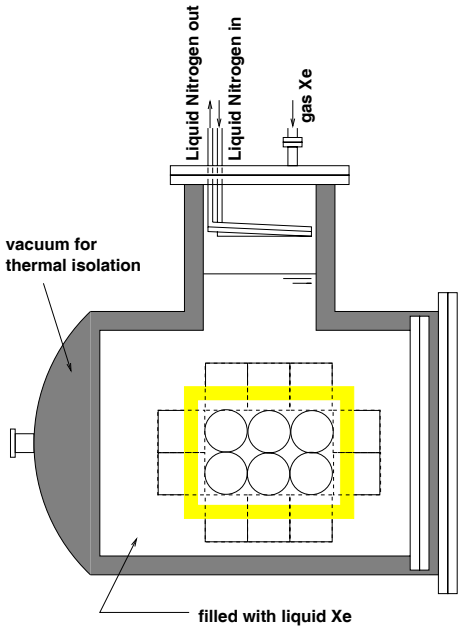

Figure 39: The layout for the prototype tests. The prototype module is placed inside liquid Xe contained in a tank.

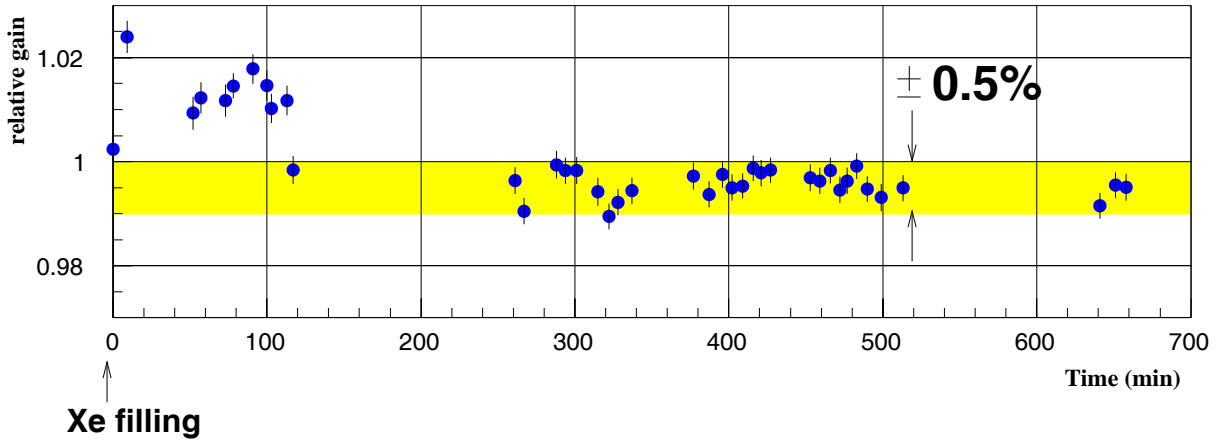

Figure 40: Time stability of PMT output from an α source.

EGS4 code [35] and incorporates all important details of the prototype module. The same off-line analysis was applied both for the real data and for the simulated data. The measured resolutions closely follow the line predicted by the simulation. This suggests that our basic understanding of the liquid Xe scintillation detector is correct, and that the simulation can provide a realistic prediction of the detector performance even for this small prototype with a small number of PMTs. The simulation should provide even more reliable predictions for the full-size detector, where the scintillation light is viewed by hundreds of PMTs, thereby averaging out various uncertainties.

The position resolution was estimated in the following way. In the offline analysis the 32 PMTs were divided into two groups by the middle x-z plane. In each group, the center position of the events (z_1, z_2) were calculated as the average of PMT positions weighted by the pulse

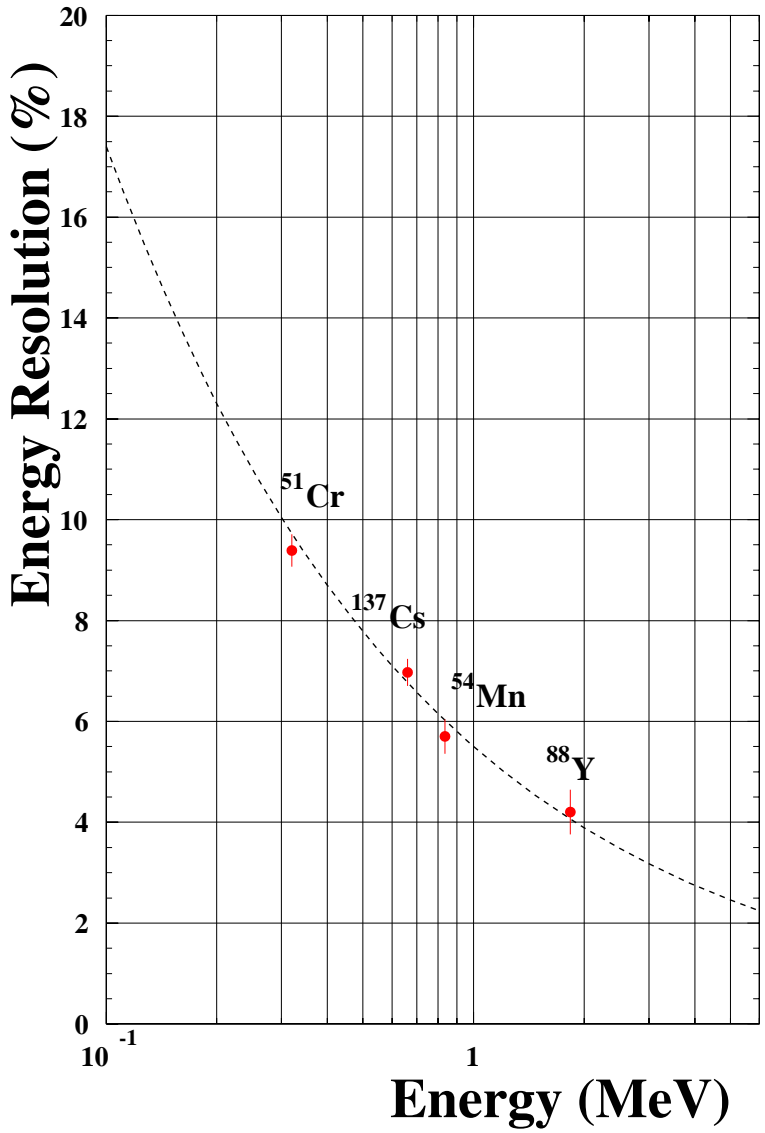

Figure 41: Energy resolution measured with the prototype, as compared to the predictions (dotted line) by the simulation.

heights. Fig. 42 shows the distributions of the difference between two positions ($\Delta_z \equiv z_1 - z_2$) for γ rays from ^{137}Cs and ^{54}Mn. Position resolutions estimated in this way are summarized in Table 4. The position resolution is about 8 mm (FWHM) around 1 MeV, and shows a tendency of decreasing with the energy.

Table 4: Position resolution for γ rays.

Nuclide	γ energy (keV)	$\sigma_{\Delta_z}/\sqrt{2}$(mm)
^{51}Cr	320	7.3 $\pm$ 0.15
^{137}Cs	662	4.3 $\pm$ 0.11
^{54}Mn	835	4.0 $\pm$ 0.13
^{88}Y	1836	2.9 $\pm$ 0.04

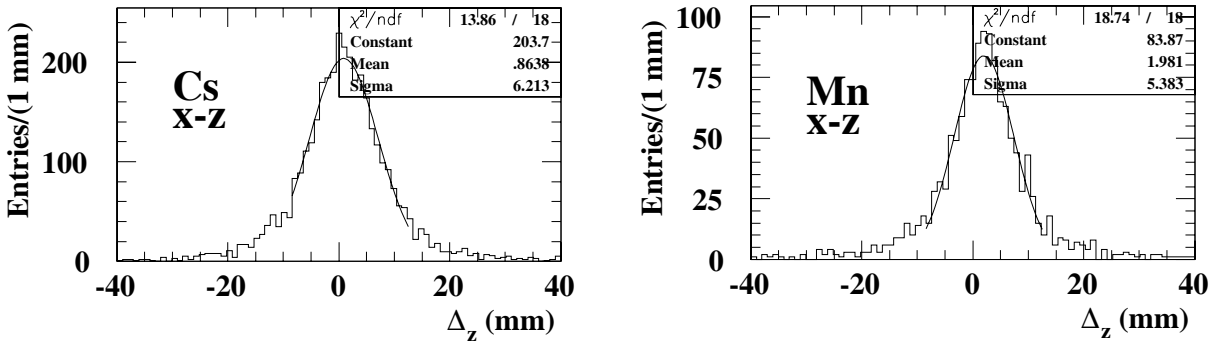

Figure 42: Distribution of $\Delta_z \equiv z_1 - z_2$ for γ rays from ^{137}Cs and ^{54}Mn.

Further R&D and the second prototype

Although the current version of PMT is already satisfactory for our purpose, better ones with higher quantum efficiencies and/or smaller sizes are being developed to improve the performance. Optimization will be finalized in one year.

If this proposal is accepted, we shall go ahead in constructing the second prototype of medium-size, which will serve as an engineering model to test various practical details necessary to be fixed before starting to construct the full-size detector.

3.3.3 Tests on PMT and Calibrations of the Detector

We consider that multi-stage tests are necessary before accepting a PMT. This is based on our experience of having operated 9,900 PMTs in the OPAL calorimeter without a single dead PMT for 11 years. We envisage following tests and measurements for each PMT.

- Test with LED light at room temperature.
- Test with LED light at –100°C.
- Measurements of quantum efficiency and gain.

The measurements have to be done with scintillation from Xe, since the UV scintillation light is difficult to simulate. During the tests on the prototype, we have invented an easy and reliable way to perform this, i.e. accumulating events from α sources in gas Xe. The broad distribution in Fig. 43 shows ADC spectrum obtained with scintillation light by α particles in gas Xe. The broadness originates from the random emission direction of α particles. In order to reduce the width, ADC mean values of every 100 events are calculated, which is shown in the figure as the hatched one. The resultant sharp peak can be used to make accurate and reliable measurements on PMT. The light from α sources is also absolutely stable and does not suffer long-term drifts common to LED or other light sources.

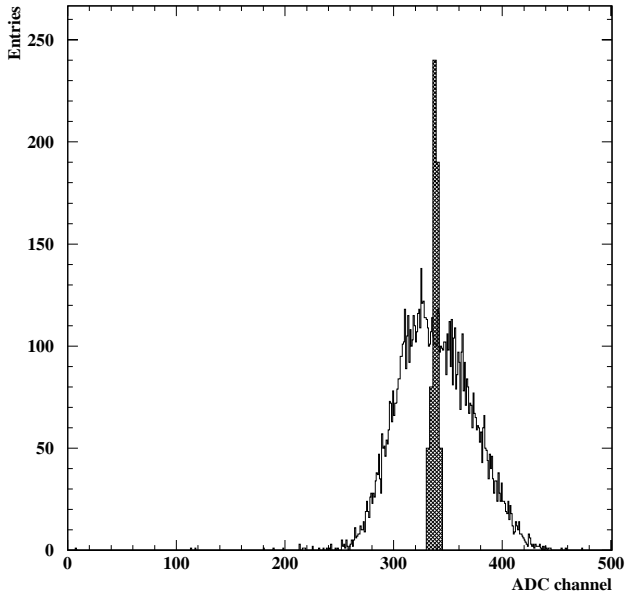

Figure 43: ADC spectrum of PMT output for scintillation light from α particles in gas Xe (broad distribution). The hatched sharp distribution is obtained by simply averaging 100 events.

PMTs which have passed these tests will be arranged into arrays.

- Test of PMT arrays with scintillation light by α particles in gas Xe as shown in Fig. 44. The α source can be moved to study the position dependence on the photo-cathode planes.

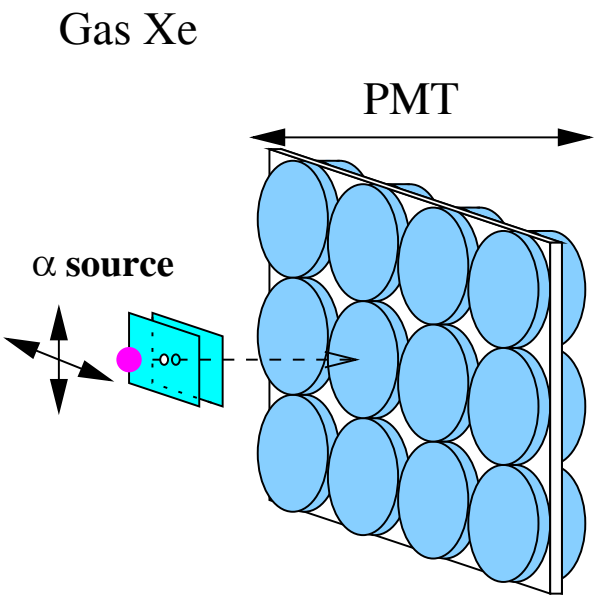

Figure 44: A schematic view of a calibration system for PMT arrays, with a movable α source in gas Xe.

After assembling the whole photon detector, measurements will be repeated by the movable α source in gas Xe, and then finally in liquid Xe.

The detector will be transported either to Tohoku University or to Budker Institute [36], where back-scattered monochromatic 52.8 MeV photon beam will be used to finally map the detector and to obtain all the calibration parameters.

For the period of full data takings at the πE5 beam line, we shall monitor the detector with LED and with movable α sources. We shall also make in-suit calibration runs with π^- beam, in which we use the sharp edges of γ ray energy from $\pi^-\mathrm{p} \rightarrow \pi^0\mathrm{n}$ process in order to absolutely calibrate the detector.

3.4 Trigger and Data Acquisition

The trigger uses the following multi-level scheme. Here we assume 1×10^8/sec muon decays on the target.

The first level trigger relies primarily on the photon detector. If we set the threshold at 42 MeV for a simple sum of the PMT signals, the rate is estimated to be 4×10^4 Hz, which is dominated by radiative Michel decays. The rate is further reduced to 2×10^3 Hz by requiring that the photon signal is in time coincidence with the positron timing-counters within 10 nsec. The rate is determined mainly by accidental coincidence between the internal bremsstrahlung and a high momentum positron from a Michel decay. When the condition of the first level trigger is satisfied, it starts the conversion process of the ADC/TDC modules, used for the photon detector and the positron timing-counters. Flash ADCs are continuously digitizing the signals from the drift chamber and the photon detector. The data are stored in ring buffer memories.

As the second level trigger, a hardware logic checks the hit pattern of the drift chamber cells against a lookup table in search of the presence of a high momentum track. A rough determination of $r - \phi$ direction of the positron track can also be obtained in this process. On the photon detector side, a hardware logic to find clusters gives us an approximate direction of the high energy photon. A back-to-back condition is then imposed on the angle between the photon and the positron. The second level trigger starts parallel readout of all data of the ADC/TDC modules and the flash ADCs. Due to a relatively small number of read-out channels, the size of an event will not exceed 100 Kbytes after zero suppression for the flash ADC data. At this level the trigger rate is expected to be sufficiently low (< 100 Hz), thereby realizing a small enough dead time. It may be possible to use also the z information of the chamber hits and/or the hit position of the timing-counter in case the expected rate reduction cannot be achieved for some reasons.

Events selected by the second level trigger are then processed by a farm of micro-processors, where we can apply selection cuts much tighter than the hardware logic can do.

High speed writing to the external mass storage will not pose a problem. A rate of 100 MB-bytes/second can be easily attained with the technology presently available. An average writing speed needed in our case, however, will be far lower than this value.

A fraction of the first level trigger will be recorded independent of the second level trigger conditions in order to make an unbiased sample, from which trigger efficiencies at a higher level can be determined.

4 Sensitivity and Background

4.1 Sensitivity

The detector acceptance defined by the positron spectrometer and the Xe detector is $0.08 < |\cos\theta| < 0.35$ and $-60^\circ < \phi < 60^\circ$, amounting to $\Omega/4\pi = 0.09$. The detection efficiency for the photon (ε_γ) is 67–75 %, depending on the E_γ cut value, while that for the positron (ε_e) is 95 %.

Assuming the muon stop rate of $N_\mu = 1 \times 10^8$ /sec and the total running time of the experiment $T = 2.2 \times 10^7$ sec, the single event sensitivity for this experiment is calculated as

$$\begin{aligned} B(\mu^+ \to \mathrm{e}^+\gamma) &= \frac{1}{N_\mu \cdot T \cdot (\Omega/4\pi)} \times \frac{1}{\varepsilon_\mathrm{e} \cdot \varepsilon_\gamma \cdot \varepsilon_{sel}} && (1) \\ &= \frac{1}{(1 \times 10^8) \cdot (2.2 \times 10^7) \cdot 0.09} \times \frac{1}{0.95 \cdot 0.7 \cdot 0.8} && (2) \\ &= 0.94 \times 10^{-14}. && (3) \end{aligned}$$

Here ε_{sel} is the efficiency of the event selection.

4.2 Background

There are two major backgrounds to the $\mu^+ \to \mathrm{e}^+\gamma$ experiment: (1) Prompt or physics background from radiative muon decays, $\mu^+ \to \mathrm{e}^+\nu_\mathrm{e}\overline{\nu}_\mu\gamma$, and (2) accidental background. The backgrounds crucially depend on detector performance. With the expected performance of our detectors, summarized in Table 5, the accidental background poses more threat than the prompt one.

It is noted that the accidental background B_{acc} is approximately given by the following formula (Appendix A):

$$B_{acc} \propto \delta E_\mathrm{e} \cdot \delta t_{e\gamma} \cdot (\delta E_\gamma)^2 \cdot (\delta\theta_{\mathrm{e}\gamma})^2 \qquad (4)$$

Our detector design is aimed at best possible improvements on δE_γ and $\delta\theta_{\mathrm{e}\gamma}$ over the previous experiments (See Table 7 in Appendix B). An ultimate timing resolution $\delta t_{\mathrm{e}\gamma}$ is also pursued to fight against any type of accidental coincidences.

In evaluating the backgrounds, it is crucial to estimate pile-up of γ rays from various sources. In the following sections pile-up photon yields are evaluated and their effects are taken into account in the background calculations. As in Appendix A, the normalized photon and e^+ energies, $x = 2E_{\mathrm{e}^+}/m_\mu$ and $y = 2E_\gamma/m_\mu$, are used.

4.2.1 Inclusive Photon Yield

To properly incorporate the effect of photon pile-up in the background estimate, inclusive photon yield per muon decay $g_\gamma(y)$ is evaluated, where $f_\gamma(\varepsilon) \equiv \int_\varepsilon^1 dy g_\gamma(y)$ is the number of photons with $E_\gamma \geq \frac{m_\mu}{2}\varepsilon$ per muon decay.

Table 5: Expected detector performance.

	FWHM
ΔE_e	0.7%
ΔE_γ	1.4% (2.0%)[*1]
$\Delta\theta_{e\gamma}$	12 mrad (14 mrad)[*2]
$\Delta t_{e\gamma}$	0.15 nsec

[*1] $z_\gamma < 2$ cm. [*2] $z_\gamma < 1$ cm.

The sources of the photons considered here include: (1) radiative muon decays, (2) annihilation in flight, (3) positron interactions in the surrounding materials, and (4) neutron interactions in liquid Xenon.

(1) Photons from radiative muon decays:

The rate per muon decay $g_{rad}(y)$ is obtained by integrating out the positron energy and the angular distribution of the differential rate [37, 38].

(2) Photons from annihilation in flight:

The rate per muon decay $g_{aif}(y)$ is given by the following formula:

$$g_{aif}(y) = \int_y^1 dx\ \sigma_{aif}(x,y)M(x)D(x), \tag{5}$$

where $\sigma_{aif}(x,y)$ is the annihilation cross section [39]; $M(x) = 6x^2 - 4x^3$ is the Michel spectrum; and $D(x)$ is the average total number of electrons per cm^2 in the material traversed by the positron with the energy fraction $x \equiv 2E_e/m_\mu$. High energy photons, which are most relevant in the background estimate, are emitted along the original positron direction. To evaluate the rate of the annihilation photons entering the Xenon volume, the value of $D(x)$ traversed by the positron moving toward the Xe volume is calculated by Monte Carlo simulations. Only materials intersected by the positrons are the target, the chamber materials, and the gas; the largest contribution comes from the target.

(3) Photons from positron interactions with surrounding materials:

According to Monte Carlo simulations, photons from this source ($g_{mat}(y)$) are mostly at low energy (< 0.5 MeV) with a sharp peak at 511 keV. They are 3–4 orders of magnitude smaller than the radiative decays.

(4) Neutron induced background:

From the neutron capture data and the calculations, it is generally concluded that neutron induced background is less severe for liquid Xenon than for NaI. Thanks to the recently conducted study on the neutron background at the πE5 beam channel [40], the neutron background seems much smaller than expected. A rough estimate shows that the neutron induced background rate is small compared to the radiative decays. As it is planned to place more shielding for the experiment, this background can be further reduced. It is therefore ignored in the following calculations.

Thus the total photon yield becomes $g_\gamma(y) = g_{rad}(y) + g_{aif}(y) + g_{mat}(y)$. The integrated yield $f_\gamma(y) = \int_y^1 dy' g_\gamma(y')$ is plotted in Fig. 45. With a δy cut of 1 %, the annihilations in flight give a largest contribution.

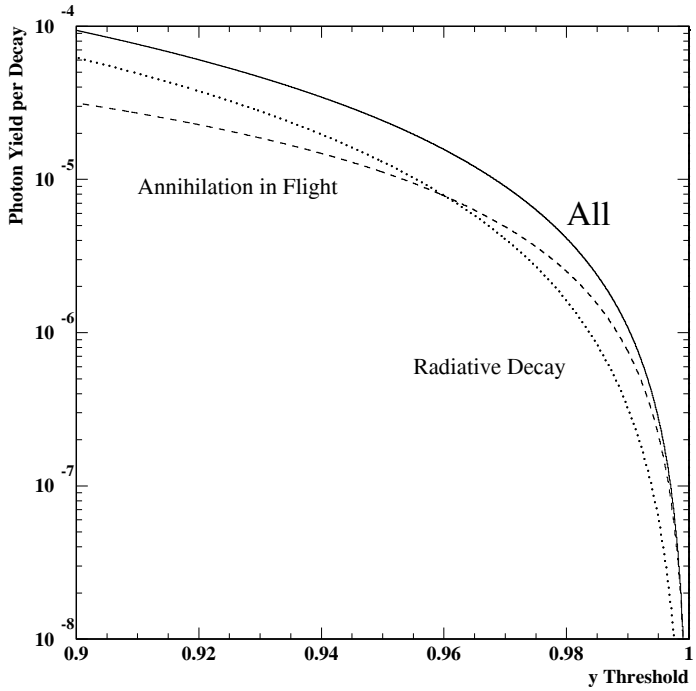

Figure 45: Integrated photon yield per muon decay $f_\gamma(y)$.

4.2.2 Photon Pile-up

Given the single photon yield $g_\gamma(y)$, the rate of two photon pile-up can be expressed as

$$g_{\gamma\gamma}(y) = \int_0^y dy' g_\gamma(y') g_\gamma(y - y') \eta(y', y - y'), \tag{6}$$

where $\eta(y_1, y_2)$ is the pile-up rejection factor for two photons with energy fractions y_1 and y_2. It can be expressed as

$$\eta = N_\mu \frac{\Delta\Omega_{\gamma\gamma}}{4\pi} \Delta t_{\gamma\gamma} \tag{7}$$

where $\Delta\Omega_{\gamma\gamma}$ and $\Delta t_{\gamma\gamma}$ define two-photon separation power in solid angle and in time respectively, and are dependent on the energies of the photons. They are evaluated by Monte Carlo simulations (See Sec. 3.3.1).

The resulting integrated pile-up photon yield $f_{\gamma\gamma}(y) = \int_y^{2-y} dy' g_{\gamma\gamma}(y')$ is shown in Fig. 46. With a δy cut of 1 %, $f_{\gamma\gamma}$ is well below the single rate[1] f_γ.

[1]Double pile-up events where three photons are in coincidence are also calculated. With a δy cut of 1 %, they are much smaller and are ignored in the following discussions.

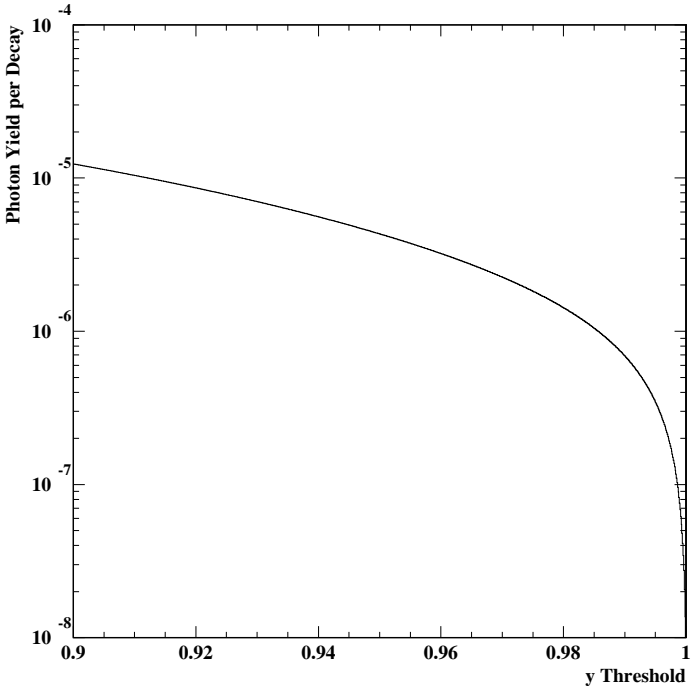

Figure 46: Integrated Pile-up photon yield per muon decay $f_{\gamma\gamma}(y)$.

4.2.3 Prompt Background

The prompt background can be calculated using the formula given in [37, 38]. However, to take the pile-up effects correctly into account, Monte Carlo simulations of radiative decays are made and photons given by $f_\gamma(y)$ are randomly added. A distribution of simulated radiative decays which corresponds to 1.0×10^{14} muon decays within the detector acceptance is shown in Fig. 47. Here the detector resolutions are incorporated. It is seen that the prompt background poses no problem in this experiment. Numerically integrating the photon yield for $0.995 < x < 1.005$, $0.99 < y < 1.01$, and $(\pi - \theta_{e\gamma}) < 8.4$ mrad, corresponding to a 90 % cut on each of the variables, the prompt background rate after these cuts becomes 8×10^{-17}.

4.2.4 Accidental Background

Monte Carlo simulations are carried out to estimate the rate of accidental coincidences of Michel positrons with random photons given by $f_\gamma(y) + f_{\gamma\gamma}(y)$. A distribution of accidental background events which corresponds to 1.0×10^{14} muon decays within the acceptance is shown in Fig. 48. Here the detector resolutions are taken into account. Numerically integrating the photon yield for $0.995 < x < 1.005$, $0.99 < y < 1.01$, and $(\pi - \theta_{e\gamma}) < 8.4$ mrad, corresponding to a 90 % cut on each of the variables, the accidental background rate after these cuts is calculated as 5×10^{-15}.

All the above calculations are based on the timing resolution of 150 psec in FWHM. As noted in the detector sections, based on our past experiences and the R&D studies being

conducted, we have a real hope for achieving a timing resolution of 100 psec or better. Because it is mainly the accidental background that would limit the experiment, an improvement in the timing resolution will be directly reflected in the ultimate experimental reach of the $\mu^+ \to e^+\gamma$ branching ratio. We therefore plan to perform all possible and necessary R&D to realize such improvements.

If such an improvement in the accidental background is realized, we will seriously consider a possibility of running the experiment with a higher rate than 1×10^8 /sec. A sensitivity below 1×10^{-14} will then become in real prospect.

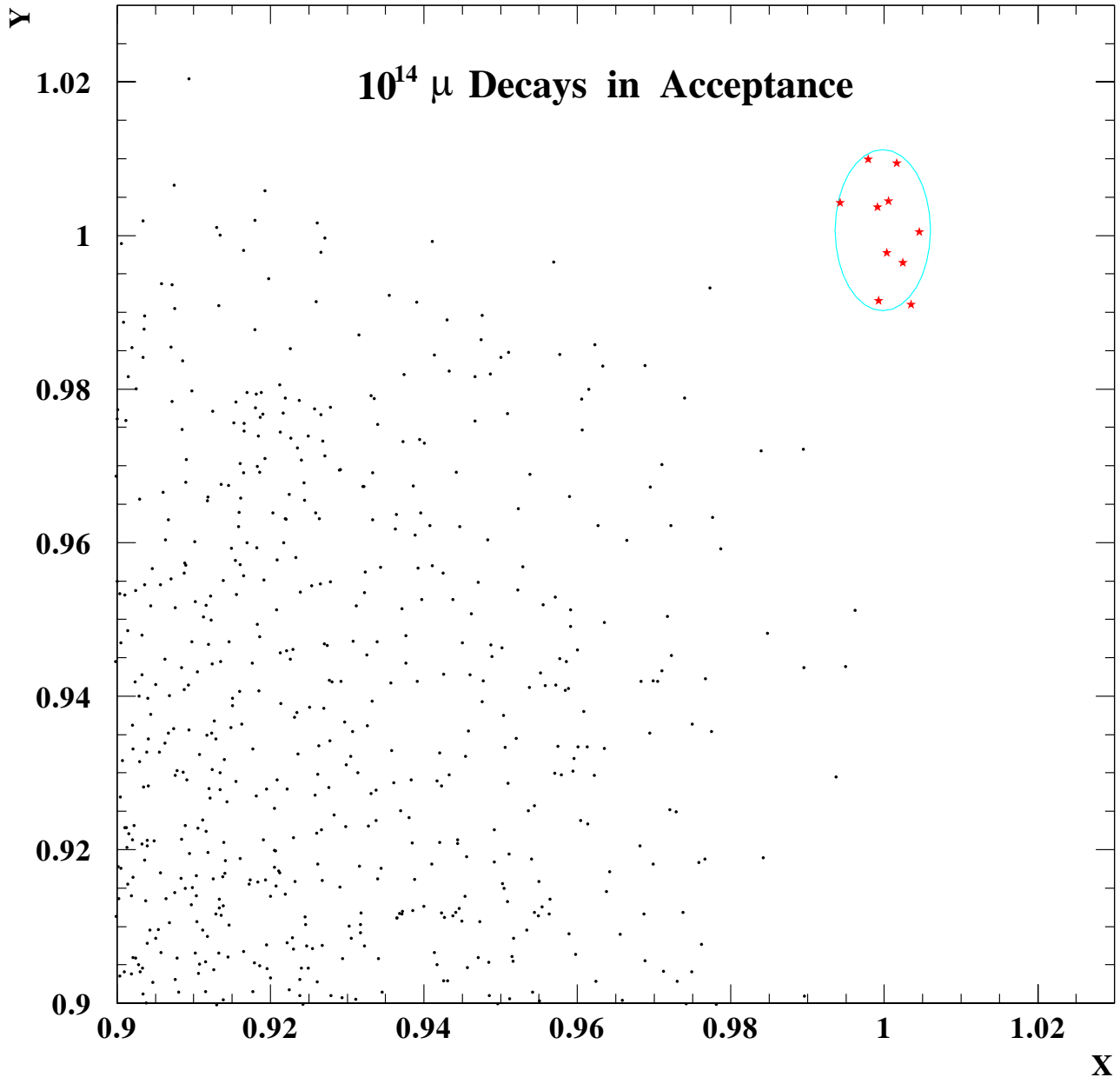

Figure 47: A distribution of simulated radiative decays after the cut $(\pi - \theta_{e\gamma}) < 8.4$ mrad for $10^{14}\mu^+$s decaying within the detector acceptance. The detector resolutions are taken into account. An expected distribution of $\mu \to e\gamma$ is also shown.

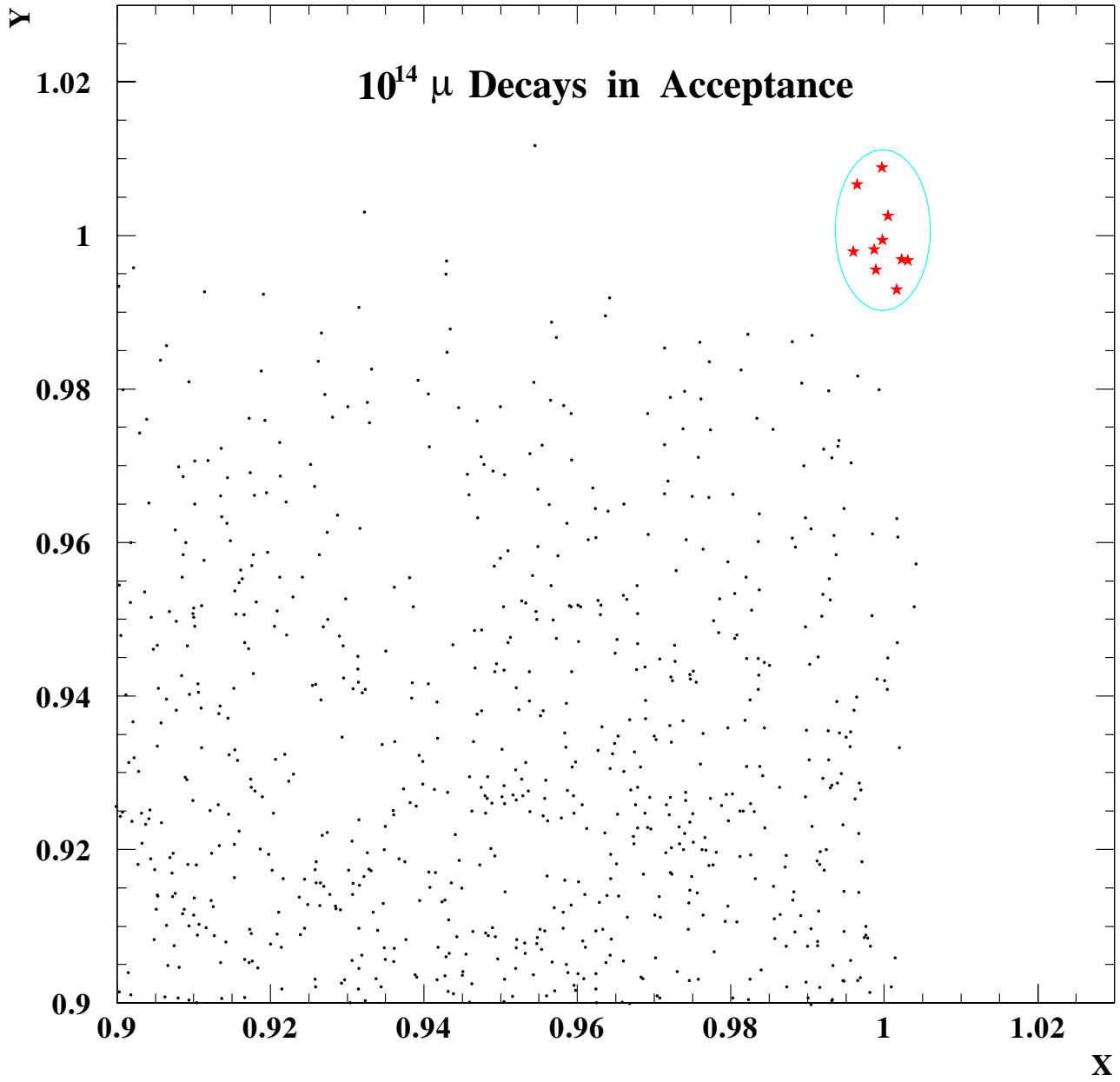

Figure 48: A distribution of simulated accidental background events for $(\pi - \theta_{e\gamma}) < 8.4$ mrad and the timing coincidence within ± 0.1 nsec for $10^{14} \mu^+$s decaying within the detector acceptance. The detector resolutions are taken into account. An expected distribution of $\mu \rightarrow e\gamma$ is also shown.

5 Cost

Out of 0.8 m^3 liquid Xe necessary, Waseda and Tokyo group already possess 0.1 m^3 of liquid Xe and shall purchase another 0.1 m^3 in 1999. Budker institute possesses 0.4 m^3 of liquid Xe, which however is allocated for another experiment. The price of liquid Xe is based on the actual purchase of 1998.

The collaboration have various items such as high voltage suppliers, electronics crates and modules, which can be utilized for this experiment. These items are not included in the cost. Present currency rate of 120 Yen/$ is assumed.

Table 6: Cost estimation

System	Item	Cost $M
Liq. Xe Scintillation Detector	Liquid Xe (0.8–0.2 m^3)	1.2
	Vessel and Refrigerator	0.2
	PMT	1.0
Drift Chamber		0.1
Timing Counter		0.2
Superconducting Solenoid		0.7
Beam Transporting Solenoid		0.2
Readout Electronics and Data Acquisition		1.2
Total		4.8

6 Acknowledgement

We wish to thank PSI people, specially D. Renker and K. Deiters, who continued to supply various information since our first visit to PSI in Nov. 1995. We thank R. E. Mischke of MEGA collaboration for very useful discussions and suggestions. Learning from MEGA experiences were crucially important in designing our experiment. Sincere thanks are to H. Sugawara and R. Eichler for their interests and supports. We are grateful to H. C. Walter, A. van der Schaaf and C. Bemporad for useful discussions. Help of K. Ozone, G. Tejima, H. Nishiguchi and Y. Kamiya are greatly acknowledged. S.O. thanks K. Maki for his contributions at early stage of conceiving and developing the concepts of the experiment. Many thanks are due to T. Yanagida, J. Hisano and D. Nomura for valuable discussions on theoretical motivations.

References

[1] R. Barbieri and L.J. Hall, Phys. Lett. **B338** (1994) 212;
R. Barbieri, L.J. Hall, and A. Strumia, Nucl. Phys. **B445** (1995) 219.

[2] Super-Kamiokande Collaboration, Y. Fukuda *et al.*, Phys. Rev. Lett. **81** (1998) 1562;
Super-Kamiokande Collaboration, Y. Fukuda *et al.*, Phys. Lett. **B433** (1998) 9 and **B436** (1998) 33;
Super-Kamiokande Collaboration, Y. Fukuda *et al.*, Phys. Rev. Lett. **81** (1998) 1158.

[3] M. Gell-mann, P. Ramond and R. Slansky, in Supergravity, Proceedings of the Workshop, Stony Brook, New York, 1979, ed. by P. van Nieuwenhuizen and D.Freedman (North-Holland, Amsterdam);
T. Yanagida, in Proceedings of the Workshop on Unified Theories and Baryon Number in the Universe, Tsukuba, Japan, edited by A. Sawada and A.Sugamoto (KEK Report No. 79-18, Tsukuba) (1979).

[4] J. Hisano and D. Nomura, Phys. Rev. **D59** (1999) 116005 and references therein.

[5] MEGA Collaboration, M. L. Brooks, *et al.*, hep-ex/9905013, submitted to Phys. Rev. Lett.

[6] A. Czarnecki, W. J. Marciano and K. Melnikov, Talk given at Workshop on Physics at the First Muon Collider and at the Front End of a Muon Collider, Fermilab, Nov. 6–9, 1997(hep-ph/9801218).

[7] MECO Collaboration, W. Molzon spokesman, *A Search for* $\mu^- N \to e^- N$ *with Sensitivity Below* 10^{-16}, AGS proposal P940, 1997.

[8] L.J. Hall, V.A. Kostelechy and S. Raby, Nucl. Phys. **B267** (1986) 415.

[9] J. Hisano, T. Moroi, K. Tobe and M. Yamaguchi, Phys. Lett. **B391** (1997) 341.

[10] R. Davis Jr., D.S. Harmer, and K.C. Hoffman, Phys. Rev. Lett. **20** (1968) 1205.

[11] K.S. Hirata et al., Phys. Rev. Lett. **63** (1989) 16.

[12] K.S. Hirata et al., Phys. Rev. Lett. **65** (1990) 1297.

[13] Y. Fukuda *et al.*, (Super-Kamiokande Collaboration), Phys. Rev. Lett. **81** (1998) 342.

[14] J. Hisano, T. Moroi, K. Tobe, M. Yamaguchi, and T. Yanagida, Phys. Lett. **B357** (1995) 579.

[15] J. Hisano, D. Nomura, T. Yanagida, Phys. Lett. B **437** (1998) 351.

[16] A. Badertscher, D. Renker and L. Simons, PSI internal report (1989);
PSI Users' Guide, Accelarater Facilities.

[17] K.L. Brown, D.C. Carey, Ch. Iselin and F. Rothacker: Transport, a Computer Program for Designing Charged Particle Beam Transport Systems. CERN 73-16 (1973) and CERN 80-04 (1980).

[18] GEANT, Detector Description and Simulation Tool, CERN Program Library.

[19] H. Matsunaga *et al.*, Phys. Rev. Lett. **81** (1998) 4052;
Y. Ajima *et al.*, submitted to Nucl. Instr. and Meth. A.

[20] Y. Shikaze *et al.*, to be submitted to Nucl. Instr. and Meth. A.

[21] A. Yamamoto *et al.* IEEE Trans, MAG-24, No.2 (1998) 1421.

[22] J. Allison *et al.* Nucl. Instr. and Meth. **A310** (1991) 527.

[23] BELLE Collaboration, BELLE Progress Report, KEK Report 97-1, April 1997;
BELLE Collaboration, BELLE Technical Design Report, KEK Report 95-1, April 1995.

[24] BaBar Collaboration, Technical Design Report, March 1995.

[25] O. Nitoh *et al.* Jpn. J. Appl. Phys. **33** (1994) 5929.

[26] R. Veenhof, Nucl. Instr. and Meth. **A419** (1998) 726.

[27] P. Billoir, Nucl. Instr. and Meth. **225** (1984) 352.

[28] T. Doke, Nucl. Instr. and Meth. **A327** (1993) 113.

[29] A. Hitachi *et al.*, Phys. Rev. **B27** (1983) 5279.

[30] S. Orito, The first workshop on $\mu \to e\gamma$ at PSI, March 1997.

[31] ATLAS Liquid Argon Calorimeter Technical Design Report, CERN/LHCC/96-41, ATLAS TDR 2, December 15, 1996.

[32] P. Benetti *et al.*, Nucl. Instr. and Meth. **A329** (1993) 361.

[33] Oxisorb is a trade mark of Messer Griesheim GmbH.

[34] R6041Q, HAMAMATSU Photonics K.K.

[35] W. R. Nelson, H. Hirayama and D. W. O. Rogers, "The EGS4 Code System", SLAC-265(1985).

[36] G.Ya. Kezerashvili *et al.*, Nucl. Inst. Meth. **A328** (1993) 506;
V.M. Aulchenko *et al.*, Proc. of the 5th International Conference on Instrumentation for Colliding Beam Physics, Novosibirsk (1990) p.68;
V.M. Aulchenko *et al.*, Nucl. Inst. Meth. **A355** (1995) 261.

[37] Y. Kuno and Y. Okada, Phys. Rev. Lett. **77** (1996) 434.

[38] C. Fronsdal and H. Überall, Phy. Rev. **113** (1959) 654;
S. G. Eckstein and R. H. Pratt, Ann. of Phys. **8** (1959) 297.

[39] W. Heitler, The Quantum Theory of Radiation, Oxford Univ. Press, London, (1954) p.267.

[40] C. Bemporad, $\mu^+ \to e^+\gamma$ meeting, PSI, March 24, 1999.

[41] Y. Kuno, A. Maki, and Y. Okada, Phys. Rev. D55 (1997) 2517.

[42] A. Van der Schaaf,*et al.*, Nucl. Phys. A **340** (1980) 249.

[43] P. Depommier *et al.*, Phys. Rev. Lett. **39** (1977) 1113.

[44] W.W. Kinnison *et al.*, Phys. Rev. D **25** (1982) 2846.

[45] R.D. Bolton, *et al.*, Phys. Rev. D **38** (1988) 2077.

A Accidental Backgrounds

In the following, accidental backgrounds are discussed. For simplicity, the normalized e^+ and photon energies, which are defined by $x = 2E_e/m_\mu$ and $y = 2E_\gamma/m_\mu$, will be used, where m_μ is a muon mass. Further, it is assumed that δA and ΔA are taken to be a half width and a full width of of the signal box for the observable A respectively.

The effective branching ratio of the accidental background (B_{acc}) can be derived. First of all, a number of the accidental background events (N_{acc}) are given by

$$N_{acc} = (N_\mu \cdot f_e^0 \cdot \frac{\Omega}{4\pi} \cdot \varepsilon_e) \cdot (N_\mu \cdot f_\gamma^0 \cdot \frac{\Omega}{4\pi} \cdot \varepsilon_\gamma) \times (\frac{\delta\omega}{\Omega}) \cdot (2\delta t) \cdot T \cdot f_{P_\mu}, \tag{8}$$

where δt is a timing coincidence resolution. f_e^0 and f_γ^0 are the fractions of the spectrum within the signal box of the e^+s in the Michel muon decay and photons in the radiative muon decay respectively. They include their branching ratios. f_{P_μ} is a background suppression factor when a muon is polarized [41]. f_{P_μ}=1 is considered from now on. The effective branching ratio for accidental background can be obtained by dividing Eq.(8) by the product of a total number of muons and the detector acceptance given by

$$B_{acc} = \frac{N_{acc}}{N_\mu \cdot T \cdot (\Omega/4\pi) \cdot \varepsilon_e \cdot \varepsilon_\gamma}. \tag{9}$$

For unpolarized muons, B_{acc} becomes

$$B_{acc} = N_\mu \cdot f_e^0 \cdot f_\gamma^0 \cdot (\frac{\delta\omega}{4\pi}) \cdot (2\delta t) \tag{10}$$

Estimation of f_e^0

f_e^0 is obtained for a given δx by integrating the Michel muon spectrum (N_{michel}) from $1-\delta x$ to 1.

$$\begin{aligned} f_e &= \int_{1-\delta x}^{1} dx N_{michel} \frac{d(\cos\theta_e)}{2} \\ &= \int_{1-\delta x}^{1} dx \left[2x^2 \Big((3-2x) + 2x^2(2x-1) P_\mu \cos\theta \right] \frac{d(\cos\theta_e)}{2} \\ &\approx 2(\delta x) \end{aligned} \tag{11}$$

Estimation of f_γ^0

To estimate f_γ^0, the radiative muon decay ($\mu^+ \to e^+ \nu_e \overline{\nu}_\mu \gamma$) is considered as a source of 52.8 MeV photon. The differential decay width is integrated over the e^+ energy and the angle between e^+ and photon ($\theta_{e\gamma}$). After the integration of e^+ energy and $\theta_{e\gamma}$, the differential branching ratio for $y \sim 1$ and any value of x is given by [41]

$$dB_{acc}(\mu^+ \to e^+ \nu \overline{\nu} \gamma) \approx J(y) \cdot (1 + P_\mu \cos\theta_\gamma) dy d\cos\theta_\gamma \tag{12}$$

where $J(y)$ is given by

$$J(y) = \frac{\alpha}{2\pi}(1-y)\Big[\ln\frac{(1-y)}{r} - \frac{17}{6}\Big] \tag{13}$$

The rate can be estimated by integrating the spectrum over the width of the signal region. The partial branching ratio (denoted by f_γ) integrated over the signal region ($1-\delta y \leq y \leq 1$) can be given from Eq.(12) by

$$\begin{aligned} f_\gamma &= \int_{1-\delta y}^{1} dy \frac{dB(\mu^+ \to e^+\nu\overline{\nu}\gamma)}{dy} \\ &\approx \Big(\frac{\alpha}{2\pi}\Big)(\delta y)^2\Big[\ln(\delta y) + 7.33\Big](1 + P_\mu \cos\theta_\gamma)\frac{d(\cos\theta_\gamma)}{2} \end{aligned} \tag{14}$$

From Eq.(14), it is shown that f_γ is roughly proportional to $(\delta y)^2$. Now, f_γ^0 that does not include the angular dependence is given by

$$\begin{aligned} f_\gamma^0 &= \Big(\frac{\alpha}{2\pi}\Big)(\delta y)^2\Big[\ln(\delta y) + 7.33\Big] \\ &= 1.16 \times 10^{-3}(\delta y)^2\Big[\ln(\delta y) + 7.33\Big] \end{aligned} \tag{15}$$

Contributions from the annihilations in flight of positrons and photon pile-ups depend on the experimental setup and are discussed in Sec. 4.

Estimation of $\delta\omega$

Given the angular resolution $\delta\theta_{e\gamma}$, the back-to-back resolution ($\delta\omega$) is presented by

$$\delta\omega = \frac{\pi(\delta\theta_{e\gamma})^2}{4\pi} = \frac{(\delta\theta_{e\gamma})^2}{4} \tag{16}$$

Net expression of accidental background

From the above, the effective branching ratio of accidental background is given by

$$B_{acc} = R_\pi \cdot (2\delta x) \cdot \Big[\frac{\alpha}{2\pi}(\delta y)^2(\ln(\delta y) + 7.33)\Big] \times \Big(\frac{\delta\theta^2}{4}\Big) \cdot (2\delta t) \tag{17}$$

where only radiative muon decays are considered as a source of photons. The detail estimation of the accidental background including contributions from annihilations in flight and photon pile-ups by using the present apparatus is given in Sec. 4.

B The Past Experiments

Experimental searches for $\mu^+ \to e^+\gamma$ has a long history since 1947, in particular they become active since the era of the meson factories (at Switzerland, U.S. and Canada). Experimental efforts have been devoted on the improvement of detection resolutions of four variables, namely the positron energy E_e, the photon energy E_γ, the timing between the positron and photon $\Delta t_{e\gamma}$, and the angle between the positron and photon $\Delta\theta_{e\gamma}$. Various kinds of apparatuses have been tried in the past history. In Table 7, the experimental results of 90% C.L. upper limit of $\mu^+ \to e^+\gamma$ decay are listed with their detector resolutions. In particular, the latest experiment, MEGA at Los Alamos National Laboratory (LANL) have reported recently their result of $B(\mu^+ \to e^+\gamma) \leq 1.2 \times 10^{-11}$ with 90 % C.L. [5].

Table 7: Historical progress of search for $\mu^+ \to e^+\gamma$ since the era of meson factories. The resolutions quoted are given as full width at half maximum (FWHM).

Place	Year	ΔE_e	ΔE_γ	$\Delta t_{e\gamma}$	$\Delta\theta_{e\gamma}$	Upper limit	References
SIN	1977	8.7%	9.3%	1.4ns	–	$< 1.0 \times 10^{-9}$	[42]
TRIUMF	1977	10%	8.7%	6.7ns	–	$< 3.6 \times 10^{-9}$	[43]
LANL	1979	8.8%	8%	1.9ns	37mrad	$< 1.7 \times 10^{-10}$	[44]
LANL	1986	8%	8%	1.8ns	87mrad	$< 4.9 \times 10^{-11}$	[45]
LANL	1999	1.2%*	4.5%*	1.6ns	17mrad	$< 1.2 \times 10^{-11}$	[5]

* shows an average of the numbers given in [5].